Magnetic Resonance Spectroscopic Imaging with 2D Spectroscopy for the Detection of Brain Metabolites

by

Trina Kok

B.Eng, Duke University, 2005
S.M., Massachusetts Institute of Technology, 2009

Submitted to the Department of Electrical Engineering and Computer Science
in Partial Fulfillment of the Requirements for the Degree of

Doctor of Philosophy

at the

MASSACHUSETTS INTITUTE OF TECHNOLOGY

September, 2012

Author_____
Department of Electrical Engineering and Computer Science
August 23rd, 2012

Certified by_____
Elfar Adalsteinsson
Associate Professor of Electrical Engineering
Associate Professor of Health Sciences & Technology
Thesis Supervisor

Accepted by_____
Leslie A. Kolodziejski
Professor of Electrical Engineering
Chairman, EECS Committee of Graduate Students

THIS PAGE INTENTIONALLY LEFT BLANK

Magnetic Resonance Spectroscopic Imaging with 2D Spectroscopy for the Detection of Brain Metabolites

by

Trina Kok

Submitted to the Department of Electrical Engineering and Computer Science on September, 2012 in Partial Fulfilment of the Requirements for the Degree of Doctor of Philosophy

Abstract

While magnetic resonance imaging (MRI) derives its signal from protons in water, additional biochemical compounds are detectable in vivo within the proton spectrum. The detection and mapping of these much weaker signals is known as magnetic resonance spectroscopy or spectroscopic imaging. Among the complicating factors for this modality applied to human clinical imaging are limited chemical-shift dispersion and J-coupling, which cause spectral overlap and complicated spectral shapes that limit detection and separation of brain metabolites using MR spectroscopic imaging (MRSI). Existing techniques for improved detection include so-called 2D spectroscopy, where additional encoding steps aid in the separation of compounds with overlapping chemical shift. This is achieved by collecting spectral data over a range of timing parameters and introducing an additional frequency axis. While these techniques have been shown to improve signal separation, they carry a penalty in scan time that is often prohibitive when combined with MRSI. Beyond scan time constraints, the lipid signal contamination from the subcutaneous tissue in the head pose problems in MRSI. Due to the large voxel size typical in MRSI experiments, ringing artifacts from lipid signals become more prominent and contaminate spectra in brain tissue. This is despite the spatial separation of subcutaneous and brain tissue.

This thesis first explores the combination of a 2D MRS method, Constant Time Point REsolved SpectroScopy (CT-PRESS) with fast spiral encoding in order to achieve feasible scan times for human in-vivo scanning. Human trials were done on a 3.0T scanner and with a 32-channel receive coil array. A lipid

contamination minimization algorithm was incorporated for the reduction of lipid artifacts in brain metabolite spectra. This method was applied to the detection of cortical metabolites in the brain and results showed that peaks of metabolites, glutamate, glutamine and N-acetyl-aspartate were recovered after successful lipid suppression. The second task of this thesis was to investigate under-sampling in the indirect time dimension of CT-PRESS and its associated reconstruction with Multi-Task Bayesian Compressed Sensing, which incorporated fully-sampled simulated spectral data as prior information for regularization. It was observed that MT Bayesian CS gave good reconstructions despite simulated incomplete prior knowledge of spectral parameters.

Thesis Supervisor: Elfar Adalsteinsson
Title: Associate Professor of Electrical Engineering and Computer Science,
Associate Professor of Harvard-MIT Health Sciences & Technology

Acknowledgements

This thesis would not have been possible without the love and support of many friends and family and I would like to make special mention of them here.

I am most grateful to my advisor Elfar Adalsteinsson. He has been a strong and encouraging presence at every step of my graduate school career. Discussions with him were always enlightening and I have benefitted a lot from his depth and breadth of knowledge. He taught me what it takes to do good science while providing me the freedom to pursue independent research. I am truly fortunate to have such a brilliant and supportive mentor.

I would like to express my sincere gratitude to my thesis committee members, Dennis Freeman and Vivek Goyal, for their constructive comments and insightful questions. They are always eager to help and they have my heartfelt appreciation for that.

My sincerest thanks go to members of the MRI group at MIT, Audrey Fan, Divya Bolar, Borjan Gagoski, Berkin Bilgic, Joonsung Lee, Joseph Cheng, Lohith Kini, Filiz Yetisir, Itthi Chatnuntawech, Paula Montesinos, Obaidah Abuhashem, Shaoying Huang, Padraig Cantillon-Murphy, Kawin Setsompop, Adam Zelinski and Arlene Wint. They are extremely supportive friends and I am glad to have gotten to know them! I also thank Colin Stultz, who shares our suite and never fails to bring a smile to the members in our lab.

For my first research project, we collaborated with Florian Eichler and Eva Ratai and I gained a lot from that experience. I thank them for being so patient, encouraging and helpful. I also wish to thank Daniel Weller, Christin Sander, Kyoko Fujimoto, Wei Zhao, Thomas Witzel and Bo Zhu for their friendship and great company, especially at the annual ISMRM meetings. I am grateful to Christina Triantafyllou, Steven Shannon and Sheeba Arnold at the McGovern Institute at MIT. They have made running experiments at MIT a much smoother process, and were always responsive to my questions.

I extend my sincere thanks to my academic advisor Muriel Medard, and Terry Orlando and Janet Fischer at the MIT graduate office. They were instrumental in helping me stay on track towards the completion of my graduation requirements.

I would like to acknowledge the support I received from friends and colleagues at the Agency of Science, Technology and Research (A*STAR) in Singapore. I embarked on this amazing journey almost ten years ago with fellow recipients of the A*STAR scholarship and have forged close friendships with some of them. In particular, I thank Rinawati Rahmat, Huanqian Loh, Yvonne Koh, Nicole Tsang, Wuisiew Tan, Zhaoru Lin, Vincent Tan, Huili Goh, Xingfang Su, Huimin Tan, Huibin Zhang, Weibin Zhang and Anjan Soumyanarayanan for

giving me advice and words of encouragement even when we are separated by thousands of miles. I look forward to seeing them again in Singapore.

I am heartily thankful to the friends outside of academia who made my Boston and MIT experience extraordinary. The instructors and students at Firebeat Dancesport Studios and on the MITBDT showed true dedication in doing what they love. There are too many to list here but I would like to thank them for helping me balance work and play. I also thank the Japanese Sports Meetup members for their friendship and for ensuring that my Sundays are always adrenaline-pumping.

The Singaporeans at MIT have given me much support and laughter. I would like to specifically thank Lynette Cheah, Kenneth Lim, Xiaojuan Khoo, Daryl Lim, Kongjie Kah, Songliang Chua, Maple Ye, Thomas Yeo and Nancy Chen for being great company and for cooking me lots of delicious Singaporean fare.

My warmest thanks are due to James Nowselski for his unwavering belief in me. He has supported me through my trials and was always there for me.

My parents and grandparents have showered me with much love and support and I owe them my deepest gratitude for that. I am grateful to my parents for giving my brother and I the best they can. Pursuing an overseas education would have been impossible without their love and encouragement. My grandpa was a fine example of life-long learning- I will forever remember him bent over his dictionary and brows furrowed in concentration. I hope this work makes you proud. I wish to thank my brother and his family for always giving me sound advice and trusting me to make my own decisions. They have made this crucial past year at MIT enjoyable and comforting. I am indebted to my extended family. Auntie Chik Yah played a crucial part in my education, always reminding me to do my best. Uncle Chik Ee and my cousins have supported me through this journey in their various ways. I dedicate this thesis to my family.

Cambridge, Massachusetts, August 2012

Trina Kok

Table of Contents

List of Figures

List of Tables

Chapter 1

Introduction and Motivation

Magnetic Resonance Imaging (MRI) is a non-invasive imaging modality that provides visual representation of soft tissue without ionizing radiation effects. MRI has advanced greatly since its invention in the 1950s and now, in addition to providing high-contrast soft tissue visualization, is used to map fiber orientation in brain tissue (Diffusion Tensor Imaging), temporal signal variations arising from functional activation (functional MRI), flow properties due to blood in vessels, and tissue biochemistry (MR Spectroscopic Imaging- MRSI).

MRSI gives a frequency spectrum of biochemical compounds, e.g. brain metabolites present in each spatial voxel of tissue. The signals from these compounds are separated in frequency from the dominant water signal via subtle shifts that depend on the chemical structure of the particular compound. It is due to this frequency shift that there is a potential for physiological evaluation and material characterization of a volume of interest. MRSI is widely applied for studying the role

of metabolites in many brain pathologies, e.g. N-Acetyl-Aspartate (NAA) is a known marker for neuronal health and its deficiency is associated with neurodegenerative diseases such as adrenoleukodystrophy (ALD) [1-3] and Alzheimer's disease [4-7]. Brain metabolites however, have very small concentration compared to water signals so that MRSI scans have intrinsically low signal-to-noise ratio (SNR) compared to conventional MRI. Metabolite concentrations are expressed in mole/liter (M). The concentrations of observable brain metabolites in vivo are typically on the order 1-10 mM compared to 50M for water. SNR is proportional to voxel size and the square root of acquisition time. This means that voxel sizes for MRSI scans are typically on the order of 1 cm^3 and take tens of minutes, while voxel sizes for structural MRI scans are on the order of 1 mm^3 and take minutes.

Beyond the limitations on voxel sizes and scan times, the dominant water signal also overwhelms the signal from the metabolites, rendering water suppression techniques necessary for detecting brain metabolites. Detection of brain metabolites are further complicated by strong lipid contamination that arises from lipid signals in the subcutaneous tissue in the skin, scalp and bone marrow of the skull. Even though the subcutaneous tissue and the brain are spatially separate, ringing artifacts from the lipid signals contaminate MRSI spectra of tissue well within the brain. These lipid signals resonate close in frequency to the 2.0ppm NAA peak and often overlap with the NAA, Glutamate (Glu) and Glutamine (Gln) signal.

However, low SNR is not the only challenge in MRSI. Line splitting caused by J-coupling between different nuclei of the same compound further reduces the SNR of the frequency spectrum of the brain metabolites. Complicated J-coupling results in multiplets for a single metabolite and these multiplets overlap with the spectra of other metabolites, making metabolite quantification and detection difficult.

In addition, complicating factors such as inherent B_0 and B_1 inhomogeneities, subject-induced magnetic susceptibility variations, RF coil design and subject motion further hamper low-SNR metabolite estimation. Other types of signal contaminations, such as patient movement, also contribute to the challenge of obtaining spectroscopic images of high quality.

The motivation of this thesis is the development of MRSI techniques for the detection of J-coupled metabolites within reasonable scan times. This thesis investigates the combination of fast two-dimensional (2D) MRSI techniques with a lipid artifact reduction algorithm implemented at 3.0T and a multi-channel receiver coil array for increased SNR. The dissertation also explores the possibility of reducing scan times by under-sampling in one of two spectral dimensions of a 2D MRS experiment.

1.1 Thesis Organization

Attempts were made to re-define acronyms and acquisition techniques so that each of the chapters is self-contained and can be read independently of the other chapters. The remainder of this thesis is as follows.

Chapter 2 provides a background overview of the theory and the acquisition methods entailing a typical MRSI experiment. Information regarding the spectral properties of metabolites NAA, Glu and Gln are also included for motivating the work in this thesis. It also contains more detailed descriptions of common 2D MRS, MRSI, and 2D MRSI methods. CTPRESS and spiral spectroscopic image encoding, which are techniques that this dissertation is based on are described at length here.

Chapter 3 presents the work done for the detection of cortical metabolites via CT-PRESS implemented with spiral encoding and incorporated with a lipid

minimization algorithm. Results from three high-resolution 1.11cc in-vivo trials are discussed in detail and compared with a standard lipid suppression technique using Outer Volume Suppression (OVS) bands for fat signal nulling.

Chapter 4 introduces the concept of compressed sensing (CS) and Bayesian CS for reconstructing randomly under-sampled data. Simulated and in-vivo under-sampled 2D MRS were reconstructed with MT Bayesian CS and its results compared with three other reconstruction methods. This chapter also investigates noise modeling by incorporating noise information in the hyper-parameters associated with MT Bayesian CS.

Finally, **Chapter 5** summarizes the contents and contributions of this dissertation and describes future possible undertakings.

1.2 Bibliographical Notes

The results from Chapter 3 have been presented in the following publications.

- T. Kok, B. Bilgic, B. Gagoski, E. Adalsteinsson, "Lipid Artifact Suppression for Detection of Cortical Metabolites in High-Resolution CTPRESS", *Proc. ISMRM*, Melbourne, 2012

- T. Kok, B. Gagoski, E. Adalsteinsson, "High Resolution 2D CTPRESS with 2D Spiral Encoding", *Proc. ISMRM*, Melbourne, 2012

- T.Kok, B. Bilgic, B. Gagoski, E. Adalsteinsson, "Detection of Cortical Metabolites with Lipid Artifact Suppression in High-Resolution CT-PRESS", *in preparation for submission to J. Magnetic Resonance in Medicine,* 2012

The results from Chapter 4 have been presented in the following publications

- T. Kok, E. Adalsteinsson, "Optimized Reconstruction Parameters for Noise Modeling in Multi-Task Bayesian Compress Sensing for 2D Spectroscopy", *Proc. ISMRM*, Melbourne, 2012

- T. Kok, B. Bilgic, E. Adalsteinsson, "Multi Task Bayesian Compressed Sensing in Sparse 2D Spectroscopy", *Proc. ISMRM*, Montreal, 2011

Other published work broadly related to the work in this thesis but not described in detail include

- T. Kok, E-M Ratai, F. Eichler, E. Adalsteinsson, "Analysis of 1H metabolite ratios using image segmentation at 7T in adult patients with X-linked adrenoleukodystrophy", *Proc. ISMRM*, Toronto, 2008

- E. Ratai, T. Kok, C. Wiggins, G. Wiggins, E. Grant, B. Gagoski, G. O'Neill, E. Adalsteinsson, F. Eichler, "7 Tesla proton magnetic resonance spectroscopic imaging in adult X-linked adrenoleukodystrophy", *Proc. ISMRM*, Berlin, 2007

- E. Ratai, T. Kok, C. Wiggins, G. Wiggins, E. Grant, B. Gagoski, G. O'Neill, E. Adalsteinsson, F. Eicheler. "Seven-Tesla Proton Magnetic Resonance Spectroscopic Imaging in Adult X-Linked Adrenoleukodystrophy", *Arch. Neurol.* 2008:65(11):1488-1494

Chapter 2

Background:
Magnetic Resonance Spectroscopic Imaging

Nuclear Magnetic Resonance (NMR) was discovered independently by Felix Bloch [8] and Edward Purcell [9] in 1946, and in the 1950's, NMR was used extensively in chemistry and physics for the evaluation of molecular structure and kinematics. In 1973, Paul Lauterbur demonstrated the possibility of using linear gradient fields to spatially map molecules in a strong magnetic field. This opened up new applications for Magnetic Resonance Imaging (MRI), particularly in medical diagnostics for imaging soft tissue without the ionizing radiation effects of X-Ray and Computed Tomography (CT) imaging.

MRI uses strong magnetic fields to provide spatial information of biological tissue. The static main field of clinical MRI scanners is typically in the range of 1.5 to 4.0 Tesla, about 30,000 to 80,000 times stronger than the earth's magnetic field. Protons, which are abundant in living tissue (e.g. in water molecules) are paramagnetic and tend to align with the magnetic field they are within. It is the

presence of this para-magnetism that allows us to manipulate signals from living tissue for creating MR images.

Images are generated in two stages, excitation and readout. In the excitation phase, energy is imparted by oscillating radio-frequency pulses (RF) played at the resonant frequencies of the protons. As the protons relax to their ground state, electromagnetic energy is released and picked up by inductive coils during the readout phase.

Gradient fields are applied to generate a magnetic field that increases in strength along one spatial direction. Spatial directions are relative to the main magnetic field with z being parallel, and x and y being perpendicular to the main field. By applying magnetic gradient fields in x, y, and z during excitation, one can selectively excite a three-dimensional volume of tissue. Magnetic gradient fields applied during the readout acquisition enable the generation of a spatial map of the received signal.

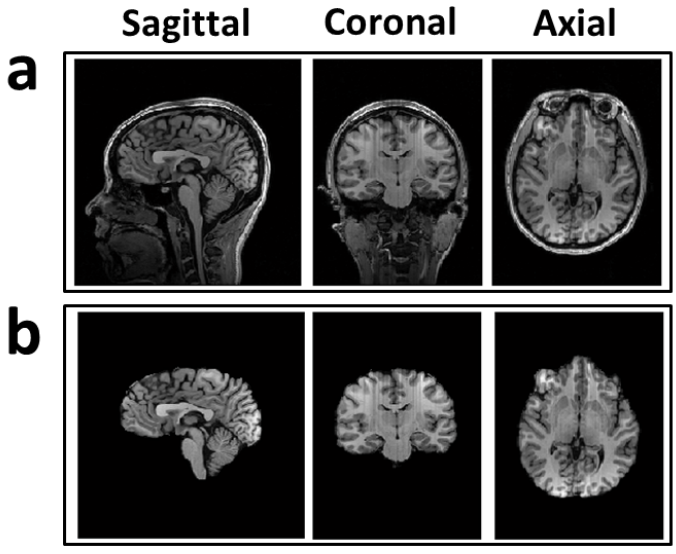

Figure 2-1: MP-RAGE images from an in-vivo experiment oriented in medical convention (a) before skull-stripping with FSL (b) after skull stripping with FSL

In displaying MRI images such as those in Figure 2-1, there are conventions about the orientations in which the images are oriented. For sagittal slices, the image is oriented as it would appear if the observer were looking at the subject's left side. Coronal slices are viewed from the subject's front as if the observer is facing the subject, and axial slices are viewed from the subject's feet with his or her anterior (front) at the top of the image. The images in Figure 2-1 are obtained with the Magnetization-Prepared Rapid Acquisition with Gradient Echoes (MP-RAGE) [10] pulse sequence and post-processed with the Oxford Centre for Functional MRI of the Brain (FMRIB) Software Library (FSL) [11, 12]. Using the brain extraction tool [13], the skull, eye orbitals, sinuses and other non-brain tissues are removed.

2.1 Magnetic Resonance Spectroscopy

Protons are present in water as well in other chemicals e.g. brain metabolites. In addition to anatomical imaging, magnetic resonance can also provide physiological and biochemical information on these metabolites via Magnetic Resonance Spectroscopy (MRS). MRS is an imaging technique where one obtains a frequency spectrum of signals, e.g. brain metabolites in vivo, from an isolated volume of tissue. MRS is based on the MR phenomenon of chemical shift, a subtle frequency shift in the signal that is dependent on the chemical environment of the particular compound.

Chemical shift is defined as a small displacement of the resonance frequency due to shielding created by the orbital motion of the surrounding electrons in response to the main static B_0 field. Protons from water and protons from individual metabolites have different resonance frequencies from one another because they experience different shielding effects.

In the presence of the main magnetic field B_0, the effective field experienced by the nucleus is:

$$B_{eff} = B_0 - B_0\sigma = B_0(1-\sigma). \quad \text{Eq. 2.1}$$

where σ represents a shielding constant dependent on the chemical environment of the nucleus. From the Larmor relationship $\omega = \gamma B$ with γ being the gyromagnetic ratio, we can write the above equation as

$$\omega_{eff} = \omega_0 - \omega_0\sigma = \omega_0(1-\sigma) \quad \text{Eq. 2.2}$$

$\omega_0\sigma$ is the displacement of the resonant frequency. Thus the change in frequency is proportional to the magnetic field B_0. By expressing this displacement in resonance frequency in units of "parts per million" (ppm) with respect to a reference frequency ω_R, the displacement in frequency can be compared across scans with different main magnetic field strengths, B_o. If the resonant frequency of the sample is ω_s, then the chemical shift δ in ppm is

$$\delta = \frac{\omega_s - \omega_R}{\omega_R} \times 10^6 = \frac{\sigma_s - \sigma_R}{1-\sigma_R} \times 10^6 \approx (\sigma_s - \sigma_R) \times 10^6 \quad \text{because } \sigma_R \ll 1 \quad \text{Eq. 2.3}$$

The reference frequency ω_R is that of tetramethylsilane, which is not found in human tissues but chosen to represent the 0 ppm point because of its stability in the presence of temperature and pH changes. The frequency axis in MRSI is displayed in ppm and for historical reasons, is such that the frequency decreases from left to right.

By placing a sample of material in a magnetic field, exciting it, recording the signal from its Free Induction Decay (FID), and then applying the Fourier Transform to the FID, the resultant MR spectrum shows resonances at different frequencies corresponding to different chemical shifts. The amount of displacement and the amplitude of the peaks in the spectrum depend on the molecular structure of the compound of interest.

2.1.1 N-Acetyl Aspartate, Glutamate and Glutamine

NAA is the second most abundant amino acid found in the brain. It is believed to be a marker of neuronal health and has been widely studied in many neurological applications e.g. brain injury [14], multiple sclerosis [15] and neuropsychiatric diseases [16, 17].

Glutamate is the most abundant amino acid found in the brain at approximately 12 mM/kg [18], and acts as an excitatory neurotransmitter. Together with its storage form Gln, Glu and Gln are also potentially important indicators of psychiatric diseases e.g. bipolar disorder [19, 20] and neurological diseases such as multiple-sclerosis [15]. This thesis focuses on resolving glutamate (Glu) and glutamine (Gln) for human brain spectroscopy at 3T.

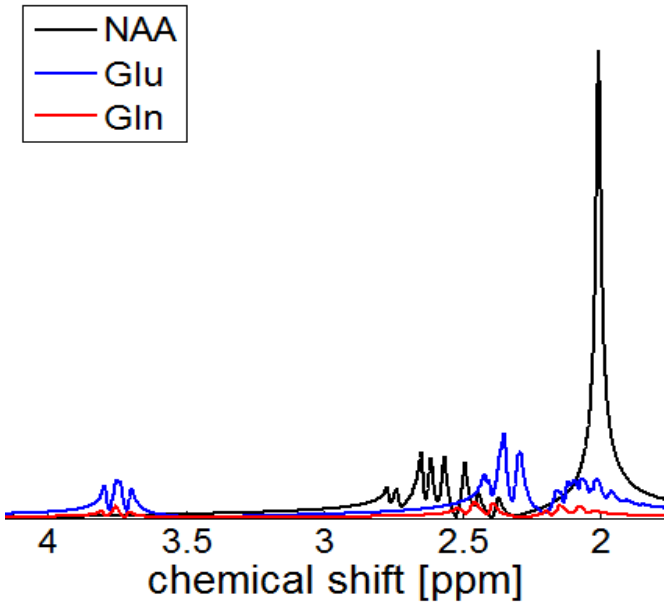

Figure 2-2: Simulated ^{1}H NMR spectrum of NAA, Glu and Gln from a spin echo pulse sequence at 3.0T and echo time (TE) = 30ms showing spectral overlap.

Metabolite	Group		Chemical shift (ppm)	Connectivity	Coupling Constant J (Hz)
N-Acetyl Aspartate	1	CH_3	2.0080		
	2	CH	4.3817	2-3	3.861
	3	CH_2	2.6759	2-3'	9.821
	3'		2.4866	3-3'	-15.592
	4	NH	7.8155	2-4	6.400
Glutamate	1	CH	3.7433	1-2	7.331
	2	CH_2	2.0375	1-2'	4.651
	2'		2.1200	2-2'	-14.849
	3	CH_2	2.3378	2-3'	8.406
	3'		2.3520	2'-3'	6.875
				2-3	6.413
				2'-3	8.478
				3-3'	-15.915
Glutamine	1	CH	3.7530	1-2	5.847
	2	CH_2	2.1290	1-2'	6.500
	2'		2.1090	2-2'	-14.504
	3	CH_2	2.4320	2-3	9.165
	3'		2.4520	2-3'	6.347
				2'-3	6.324
				2'-3'	9.209
				3-3'	-15.371

Table 1: Chemical shifts and coupling constants of protons in NAA, Glu, Gln as reported in [18] which are used in simulation studies in Chapter 4

Figure 2-2 shows the ^{1}H spectrum of N-acetyl aspartate (NAA). This spectrum is simulated at 3.0T using the SPINEVOLUTION software package. The three protons of the N-acetyl CH_3 group provides the most prominent resonance at 2.0080ppm. The three doublet-of-doublets centered at 2.4863, 2.6727ppm and 4.3817ppm arise from the protons of aspartate CH_2 and CH groups. The protons of the CH_3 group experience less shielding compared to the protons in the CH_2 and CH groups, so that the resonant frequency for CH_3 deviates less from the reference frequency at 0ppm. It also has an amide proton in the NH group which gives a

doublet at 7.8205ppm (not shown in figure). The coupling constants and chemical shifts are summarized in Table 1.

Glu has four protons in two methylene groups at 2.0375ppm, 2.1200ppm, 2.3378pm and 2.3520ppm, and one proton in a methine group at 3.7433ppm that are strongly coupled with one another, giving a complex spectrum at 3T with low-intensity multiplets. The Glu spectrum overlaps with resonances of Gln, γ-Aminobutyric acid (GABA) and NAA, making detection and in-vivo quantification difficult.

Gln is a storage form of Glu and is present in the range of 2-4 mM/kg [14]. Gln has four protons in two methylene groups at 2.1090ppm, 2.1290ppm, 2.4320ppm and 2.4540ppm and another proton in a methine group at 3.7530ppm that are strongly coupled at 3T. The coupling constants and chemical shifts of Glu and Gln as reported from Ref.[14] are also summarized in Table 1.

Due to the many overlapping multiplets of Glu and Gln, separation of Gln and Glu is very difficult at low field. Figure 2-2 also shows the simulated spectra of Glu and Gln and illustrates the spectral overlap of many of the resonances from Glu, Gln and NAA.

2.1.2 Water Suppression

Water is the most abundant source of protons in human tissue and thus its signal is dominant in an MRS spectrum and much higher than that of brain metabolites. Figure 2-3a shows an MRS spectrum from an in-vivo trial where water signal was not suppressed and Figure 2-3b shows the same experiment done with water suppression. It is important to suppress as much of the water as possible in order to see frequency peaks of the brain metabolites in an MRS spectrum. CHEmical Shift Selective imaging (CHESS) and Water suppression Enhanced through T_1 effects (WET)

are common techniques applied before the excitation part of an MRS pulse sequence for water suppression.

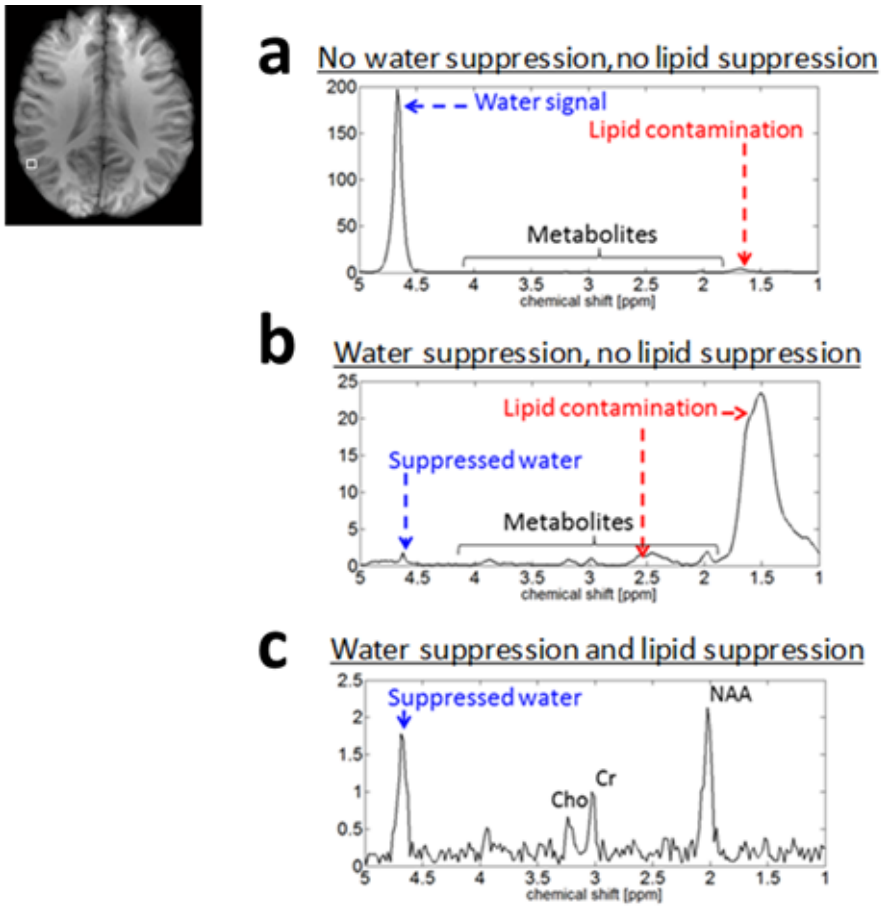

Figure 2-3: In-vivo spectra obtained with PRESS at TE = 151ms, scan time = 56s from a 1.11cc voxel at location specified in structural image. All spectra are scaled to the amplitude of the creatine (Cr) peak at 3.0ppm. (a) Spectrum obtained without suppression of water or lipids. (b) Spectrum obtained with the suppression of water and without lipid suppression. (c) Spectrum obtained with the suppression of water and lipids.

In CHESS, a spectrally-selective 90° pulse is played so that most of the water signals are brought to the transverse x-y plane, leaving negligible amounts of longitudinal components in the z direction. A spoiler gradient immediately follows and de-phases the transverse signals. The excitation pulse played after the spoiler gradient

excites only a small residual water signal along the z-direction, and water suppression is achieved.

In WET, a series of spectrally selective RF pulses are played τ milliseconds apart to incrementally decrease the transverse z component of the water signal. The optimal set of flip angles of the RF pulses for uniform water suppression across the brain are determined from field maps and T_1 values of brain tissues.

2.1.3 Lipid Suppression

Lipids exist in the subcutaneous tissues of the skin, scalp and bone marrow in the skull and have a much higher concentration than metabolites in the brain, severely hampering the detection and estimation of brain metabolites. Even though the subcutaneous tissues and the brain are spatially separate, side-lobe ringing from the impulse response of the image encoding yield severe lipid artifacts in the metabolite spectra of tissue near the skull. The spatial resolution of MRS and MRSI is limited by the low SNR of metabolite signals, leading to voxel sizes on the order of ~cm^3 compared to voxel sizes on the order ~mm^3 for structural MR imaging. The combination of large voxel sizes and strong lipid signals result in prominent ringing artifacts, which contaminate spectra inside the brain despite clear separation of brain and skull. Figure 2-3b shows a spectrum without lipid suppression, where lipid artifacts can be observed between 0.8-1.9ppm and between 2.2ppm-2.8ppm. These lipid ringing artifacts are removed from the spectrum in Figure 2-3c after the application of Outer Volume Suppression (OVS) bands.

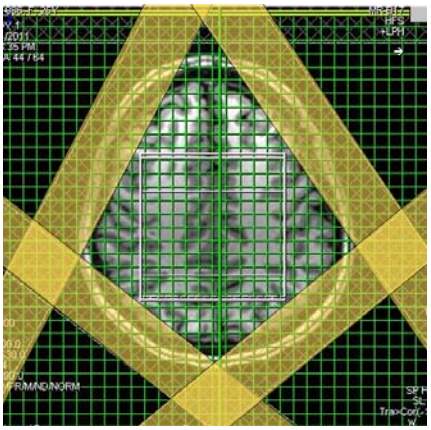

Figure 2-4: OVS bands (highlighted in yellow) are applied along the skull to null out lipid signals. The white rectangle indicates tissue volume excited. Signals from tissue near the skull are traded off for lipid suppression.

Methods such as OVS [21-24] and inversion-recovery [25-27] can be used to effectively suppress lipid signals. Figure 2-4 shows an example with OVS bands applied around the brain tissue. OVS pulses are spatially selective and played to saturate signal from the skull. However their placement and the restriction of a rectangular volume of interest during excitation means that signals from the peripheral brain tissue close to the skull must be traded off to suppress lipid signals.

In inversion recovery (IR), spins across all frequencies and space are inverted to the negative z direction by a non-selective inversion adiabatic pulse. Excitation pulses are then played at inversion time (TI) when all lipid signals are in the transverse component and signals in the longitudinal direction are close to zero. TI is determined from the T_1 relaxation time constant of the lipids. Since the inversion pulses are non-selective, they indiscriminately invert the metabolite signals as well causing metabolite signal-to-noise-ratio (SNR) loss of about 15-20%.

Spectrally selective adiabatic pulses can be used during IR to invert only lipid signals so that most of the signals are nulled when the excitation pulses are played, and

successful lipid suppression has been demonstrated at 7.0T [28]. However this method relies on sufficient spectral separation between lipid and metabolite peaks, which might be difficult at lower field strengths of 3.0T where the lipid and metabolite peaks are typically less than 100Hz apart.

Variable density spiral trajectories with matched apodization filters have been proposed to reduce the magnitude of spatial side lobes in the spatial impulse response [29] and successful lipid suppression without SNR loss has been demonstrated for this method.

2.2 2D Magnetic Resonance Spectroscopy

In addition to chemical shifts caused by the shielding of electrons, subtle chemical shifts also result from J-coupling effects within molecules. Proton nuclei that are close to one another in chemical shift exert an influence on each other's magnetic field and this influence is known as J-coupling. Coupling between nuclei causes line splitting that complicates the appearance of a 1D spectrum and reduces the available SNR.

Here we discuss an example of weak J-coupling and the line-splitting that results from it. Consider a molecule containing two different spin-½ nuclei, A and M, where their nuclei could be either spin-up (+½) or spin-down (-½). In the case of a proton nucleus, the spin-down (-½) has the lowest energy. After excitation, a proton nucleus moves from spin-down (-½) to spin-up (+½). The proton nucleus releases this energy during readout data acquisition as it transitions back to the spin-down (-½) state. Without any J-coupling, there is only one energy transition as either nucleus A or M moves from +½ to -½. This energy transition is reflected in Figure 2-5a where there is a peak in the frequency spectrum at each of the chemical shifts, ν_A and ν_M of nuclei A and M respectively.

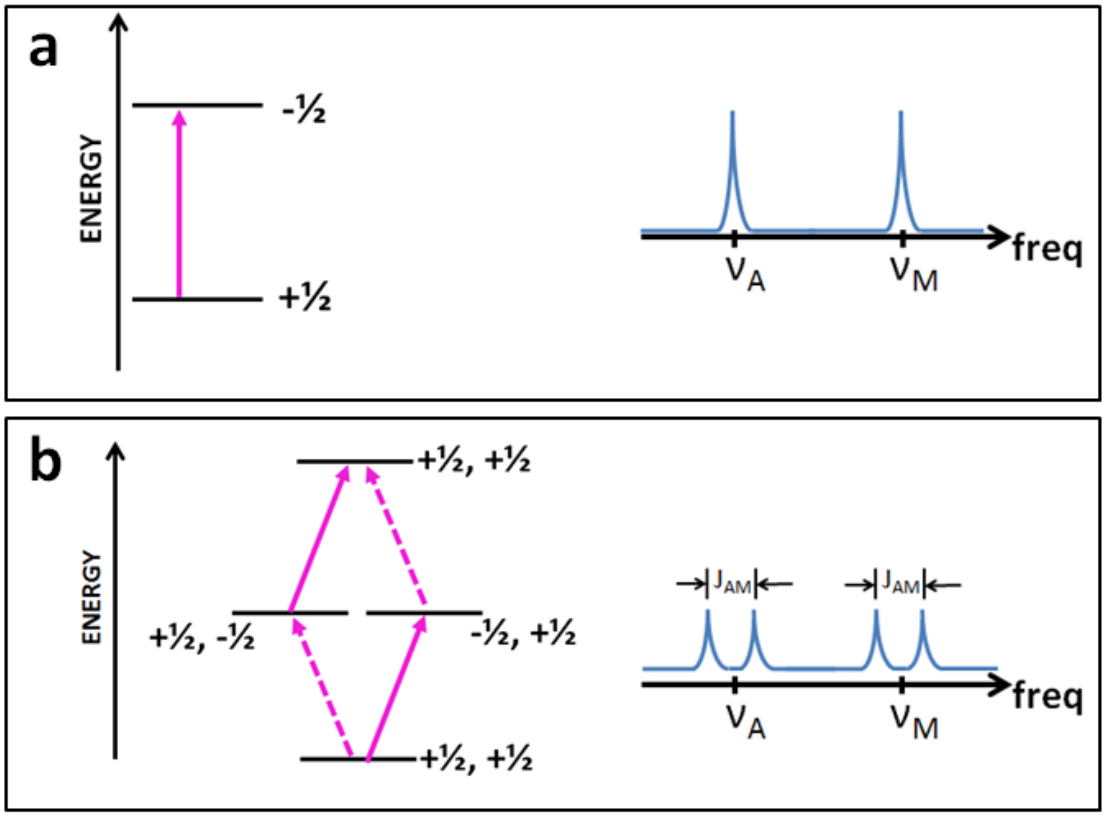

Figure 2-5: (a) Energy transitions for a single spin and the corresponding singlet lines of resonance in the frequency spectrum. (b) Energy transitions for two spins that are weakly coupled and the doublet lines of resonance separated by the coupling constant J_{AM}. The dotted line indicates energy transitions for nuclei A and the solid line indicates energy transitions for nuclei M.

Figure 2-5b shows the available spin configurations when two nuclei are coupled. Only one spin-up/spin-down change is allowed in a transition, so the four possible spin configurations of A and M results in four different transitions- two for nucleus A and two for nucleus M. The frequency spectrum exhibits two peaks with reduced amplitudes centered at the chemical shifts, ν_A and ν_M of nuclei A and M respectively instead of the single peak in Figure 2-5a. This effect is known as line-splitting and the frequency separation of the peaks is determined by the J-coupling constant J_{AM}. More complicated line-splitting occurs as more nuclei are coupled to one another through weak and strong coupling. It is possible to work out the resultant

frequency spectrum by hand or computer simulation but this is beyond the purpose of this thesis. The interested reader is directed to texts on 2D MRS for a more thorough analysis [30, 31].

Spectral editing is a method of suppressing or enhancing metabolite signals by using its spin-spin coupling properties. Due to the effects of J-modulation, different timing parameters result in different metabolite spectra that can be manipulated to resolve the metabolite of interest. Spectral editing has been exploited in [32] to resolve Glu from an in vivo spectrum at 1.5T by the subtraction of metabolite spectra from echo time (TE) = 12ms and TE = 60ms. However, spectral editing techniques have to be tuned appropriately to the metabolite of interest and cannot simultaneous detect different coupled metabolites.

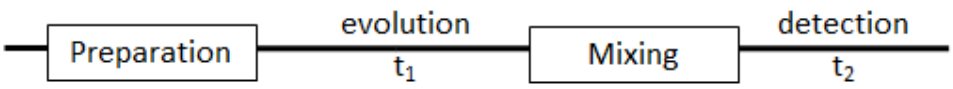

Figure 2-6: General Scheme of a 2D MRS pulse sequence

Two-dimensional (2D) MRS is a technique that introduces a second frequency axis, so that the 2D frequency spectrum reveals coupling information between different metabolites. By notational convention, ω_2 (or f_2) is used to resolve chemical shift, while ω_1 (f_1) encodes additional physical characteristics of the underlying spins, often J-coupling or a combination of J-coupling and chemical shift. The time variables corresponding to ω_1 and ω_2 are t_1 and t_2. The general scheme for a 2D MRS experiment is shown in Figure 2-6. During preparation, the tissue is excited by one or more RF pulses and the resultant magnetization is allowed to precess freely in t_1. During mixing, the tissue is again excited by one or more pulses and the FID is

detected during t_2. The precise meaning of the additional frequency axis t_1 and ω_1 depends on the kind of experiment performed.

There exist a number of different 2D MRS experiments, and this thesis will focus on the Constant Time Point Resolved Spectroscopy (CT-PRESS) to attempt to resolve Glu and Gln for human brain spectroscopy at 3T.

2.2.1 Correlated Spectroscopy

The pulse sequence for a Correlated Spectroscopy (COSY) [33, 34] experiment consists of two 90° pulses each played during preparation and mixing. The first 90° pulse flips the magnetization to the transverse x-y plane where it evolves under the influences of both chemical shift and J-coupling during t_1. The second 90° pulse is used for coherence transfer between J-coupled metabolites.

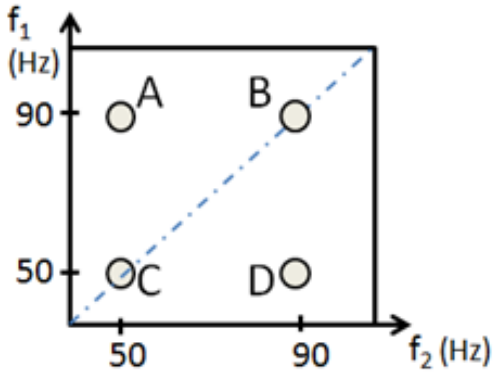

Figure 2-7: Cartoon representation of a COSY 2D spectrum with diagonal and cross peaks

Figure 2-7 shows a cartoon representation of a 2D COSY spectrum and we first look at cross-peak 'A'. The cross-peak 'A' at (f_1 = 90Hz, f_2 = 50Hz) indicates that a signal evolving at 90Hz during t_1 was transferred by the second 90° pulse to another signal which evolved at 50Hz during t_2. Similarly, the cross-peak 'D' at (f_1 = 50Hz, f_2 = 90Hz) indicates the transfer of a signal evolving at 50Hz during t_1 to a signal evolving at 90Hz during t_2. In this way, the cross peaks indicate coupling between the nuclei at

chemical shifts of 50Hz and 90Hz. The diagonal peaks 'B' and 'C' just indicate the presence of two nuclei evolving at 50Hz and 90Hz throughout t_1 and t_2. Coupling information is encoded in cross peaks symmetrical along the diagonal of the 2D spectrum.

A volume selective version of COSY, Localized-COSY (L-COSY) [35] introduces an additional 180° pulse after the first 90° pulse during preparation, exciting a 3D volume by playing magnetic gradients with the three pulses. While COSY-type methods are useful for identifying the coupling networks within a molecule, it suffers from reduced sensitivity because of the transfer of metabolite signals onto cross peaks.

2.2.2 J-resolved MRS: 2D JPRESS

In J-resolved MRS [36-38], the pulse sequence consists of a spin echo module i.e. a 90° pulse is played during preparation and a 180° pulse is played during mixing, so that data is acquired as a function of t_1 = echo time (TE) and t_2. After the 90° pulse, magnetization is transferred to the transverse plane and evolves with chemical shift and J-coupling. All de-phasing that occurred during t_1 due to chemical shift are refocused by the 180° pulse. In this way, t_1 encodes only J-coupling information. After the 180° pulse is played and chemical shift effects from t_1 are refocused, signal continues to evolve with J-coupling and chemical shift during t_2.

To enable a volume selective experiment, an additional 180° pulse is applied after the 90° pulse during preparation. Gradient magnetic fields played during the three excitation pulses select for a volume in the x, y and z plane respectively. These three pulses (90° -180° -180°) make up the PRESS module commonly used in 1D spectroscopy for volume localization, and the 2D MRS technique is known as 2D JPRESS.

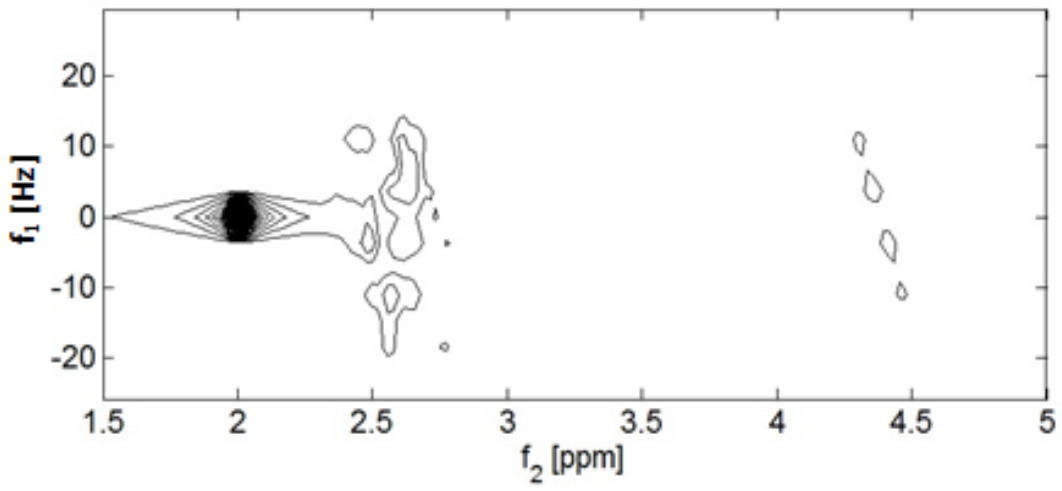

Figure 2-8: 2D JPRESS spectrum before 45° tilt with 16 TE values, starting at 17ms and incremented in steps of 17ms. Spectrum was simulated at 3.0T with SPINEVOLUTION.

A simulated 2D JPRESS spectrum of NAA is shown in Figure 2-8. Because J-coupling manifests itself in both f_1 and f_2, the spectrum for coupled spins is tilted along the 45°-axis in the (f_1, f_2) plane. This 45° tilt is especially clear in the doublet-of-doublets centered at 4.38ppm in Figure 2-8. In post-processing, the 2D spectrum is tilted by 45° along the diagonal to obtain only the J-coupling information in f_1 and chemical shift information in f_2.

Since f_1 encodes only J-coupling information, the 2D JPRESS spectrum does not have cross peaks. Instead, the spread of multiplets are seen in only f_1 and the chemical shift of each proton nuclei group is seen in f_2 after a 45° post processing tilt of the 2D spectrum. While such a 2D spectrum does not provide information about spin-spin coupling, a decoupled 1D spectrum could be obtained by taking the magnitude projection along the f_1 axis onto the f_2 axis so that the multiplets collapse into a single peak on f_2. Other manipulations of the 2D JPRESS spectrum include taking the $f_1 = 0$ component as an average across all the TEs for reliable detection of Glu [39].

2.2.3 Constant Time PRESS

CT-PRESS [40, 41] is a 2D MRS method very similar to 2D JPRESS. It consists of a PRESS module for volume selection and an additional non-selective refocusing 180° pulse whose position is shifted within a constant time interval between the RF excitation pulses and signal acquisition. The extra 180° pulse was first introduced because of an imperfect slice profile selected with PRESS and insufficient spoiler gradients. In theory, the position of the last spatially selective 180° pulse could also be used to encode t_1.

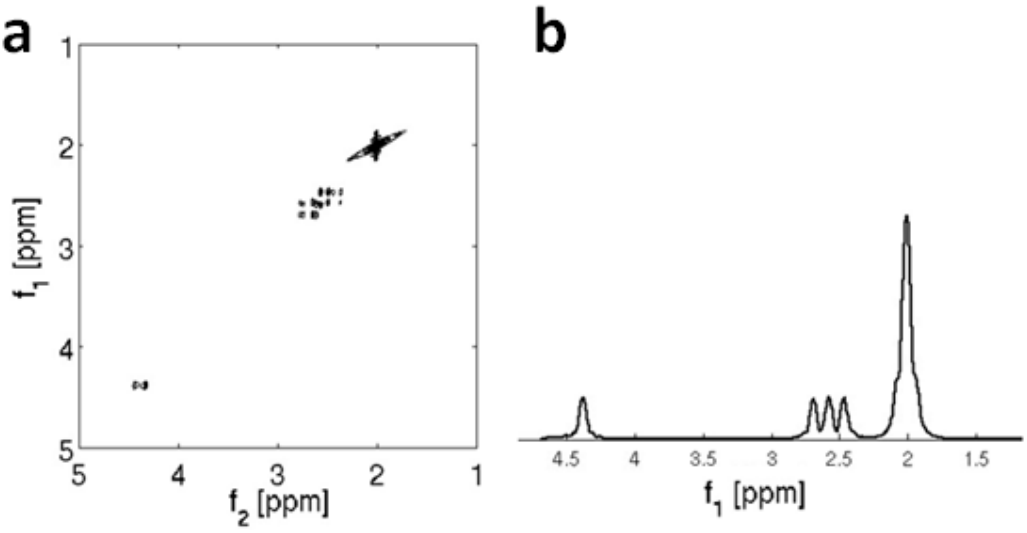

Figure 2-9: (a) CT-PRESS spectrum of NAA at 3.0T with 129 t_1 steps, with TE starting at 48.6ms and incremented in steps of 1.6ms. Spectrum was simulated with SPINEVOLUTION. (b) Decoupled spectrum of NAA obtained by projecting 2D spectrum along f_2 onto f_1.

Since the time interval between excitation and acquisition is kept the same for each t_1 step, modulation by J-coupling remains the same and line splitting in f_1 is suppressed. Like in 2DJPRESS, magnetization is not transferred to the cross-peaks and they are eliminated in the 2D Fourier representation. All magnetization is instead transferred to the diagonal spectrum which contains signals of all uncoupled spins and

diagonal peaks of coupled spins. Figure 2-9a shows the diagonal pattern of the 2D CT-PRESS spectrum of NAA and the reduced line splitting in f_1 which is best illustrated by the doublet-of-doublets peaks centered at 4.38ppm. Since line-splitting is only manifested in f_2, a decoupled 1D spectrum can be obtained by taking the projection of the 2D spectrum in f_2 onto f_1. Figure 2-9b shows the decoupled spectrum corresponding to the 2D spectrum of NAA in Figure 2-9a. Comparing this decoupled spectrum of NAA to Figure 2-1 obtained with 1D spectroscopy, the multiplets centered at 2.49 and 2.67ppm have collapsed into three frequency peaks and the multiplet centered at 4.38ppm has collapsed into a single peak at 4.38ppm.

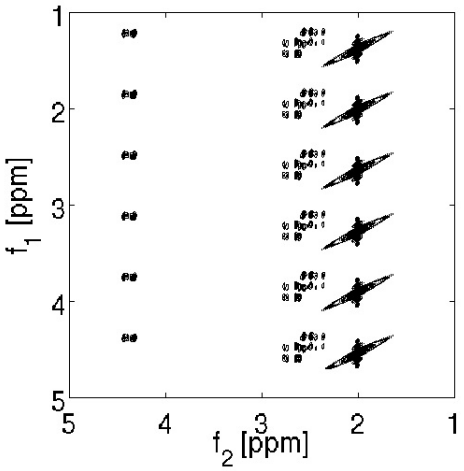

Figure 2-10: CT-PRESS spectrum of NAA at 3.0T with 17 t_1 steps, with TE starting at 48.6ms and incremented in steps of 12.8ms. Spectrum was simulated with SPINEVOLUTION. Non-overlapping aliasing is observed.

Because chemical shift is encoded in both f_1 and f_2, CT-PRESS requires a considerably larger number of t_1 steps compared to 2DJ-PRESS. About 128 t_1 steps are required for a ^{1}H chemical shift range of 5-10ppm with sufficient spectral resolution. It is possible to reduce the number of t_1 steps by noting that signals are only present near the diagonal of the 2D CT-PRESS spectrum. Some aliasing is tolerable, so sampling

below the Nyquist sampling can be adequate. This has been demonstrated by Mayer et al to achieve eight-fold under-sampling with a 17-step CT-PRESS sequence [42]. Figure 2-10 shows the aliasing introduced by under-sampling eight-fold in t_1 of the same 2D CT-PRESS experiment that gave Figure 2-9a. By summing signal along the diagonal for some frequency range in f_2, the 1D decoupled spectrum shown in Figure 2-9b can be obtained.

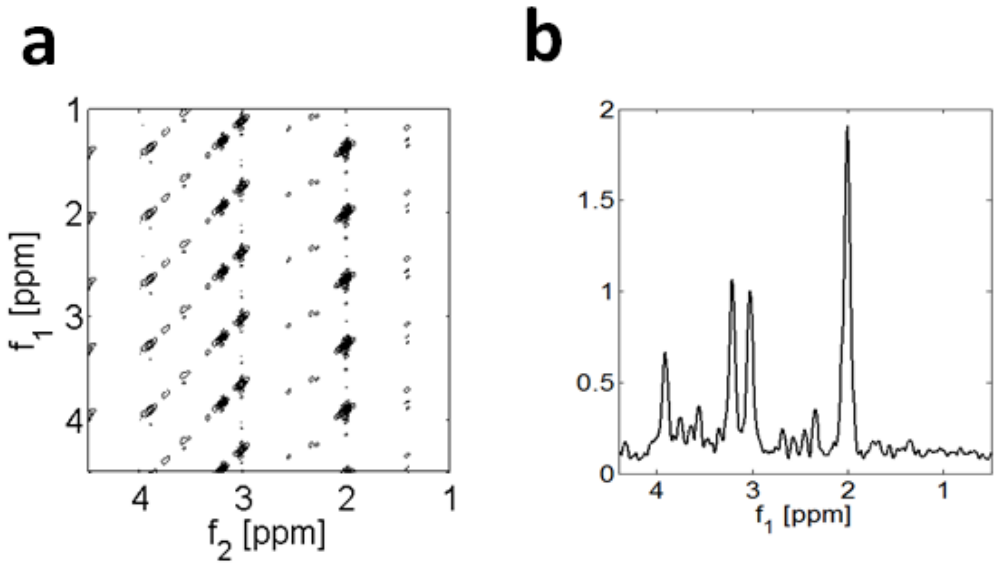

Figure 2-11: (a) 2D CT-PRESS spectrum from an in-vivo experiment at 3.0T with 17 t_1 steps, with TE starting at 48.6ms and incremented in steps of 12.8ms. Voxel size = 1.11cc and total scan-time = 13:44min. (b) Corresponding diagonal spectrum normalized to amplitude of creatine (Cr) peak at 3.0ppm

Note that since the diagonal spectrum is obtained by summing signal from the 2D spectrum in magnitude mode, noise in the diagonal spectrum does not follow a zero-mean Gaussian distribution. Figure 2-11 shows a 2D spectrum and its corresponding diagonal spectrum obtained from an in-vivo experiment. Noise in the diagonal spectrum is Rayleigh distributed with a non-zero mean so that the diagonal spectrum is offset from the zero amplitude level. CT-PRESS has been demonstrated to

detect coupled resonances with high SNR and average TE could be optimized for increased SNR of Glu. The bulk of the work in this thesis is based on the 17-step CT-PRESS variant introduced by Mayer et al. [42].

2.3 Magnetic Resonance Spectroscopic Imaging

Magnetic field gradients can be applied to spatially map the FID acquired during the readout phase of an MRS experiment. An MRS imaging (MRSI) experiment is established as spatial encoding is enabled. Here we first introduce the basic principles of an MRI experiment resolved in (x, y, z) and extend the concepts for an MRSI experiment resolved in the 4D space of (x, y, z and f).

2.3.1 Signal Equation

In MRI, applying time-varying gradient fields $G_x(t)$, $G_y(t)$ and $G_z(t)$ along x, y, and z slightly alters the local magnetic field B at each (x, y, z) location so that:

$$B(x,y,z,t) = B_0 + G_x(t)\cdot x + G_y(t)\cdot y + G_z(t)\cdot z\,. \qquad \text{Eq. 2.4}$$

The signal detected from a receiver coil is a voltage induced by flux changes from the precessing magnetization in the transverse plane. Assuming the receiver coil is uniformly sensitive in space, this signal is the sum or integral of all the spins over the entire volume of the object.

$$s(t) = \int_x \int_y \int_z m(x,y,z)\,dx\,dy\,dz \qquad \text{Eq. 2.5}$$

A spatially and time varying phase $\varphi(x,y,z,t)$ is imparted on the spins:

$$m(x,y,z,t) = m_0(x,y,z)\,e^{-i\varphi(x,y,z,t)} \qquad \text{Eq. 2.6}$$

where:

$$\varphi(x,y,z,t) = \int_0^t \omega(x,y,z,\tau)\, d\tau = \gamma \int_0^t B(x,y,z,\tau)\, d\tau. \quad \text{Eq. 2.7}$$

Substituting in Eq. 2.4 gives:

$$\varphi(x,y,z,t) = \gamma B_0 t + \gamma \left(\int_0^t G_x(\tau) d\tau \cdot x + \int_0^t G_y(\tau)\, d\tau \cdot y + \int_0^t G_z(\tau)\, d\tau \cdot z\right) \quad \text{Eq. 2.8}$$

so that:

$$s(t) \quad \text{Eq. 2.9}$$
$$= \int_x \int_y \int_z m_0(x,y,z)\, e^{-i\omega_0 t}\; e^{-i\gamma\left(\int_0^t G_x(\tau)d\tau\cdot x + \int_0^t G_y(\tau)d\tau\cdot y + \int_0^t G_z(\tau)d\tau\cdot z\right)}\, dx\, dy\, dz.$$

Here $e^{-i\omega_0 t}$ is dropped (assuming demodulation by ω_0) and the variables k_x, k_y and k_z are defined as:

$$k_x(t) = \frac{\gamma}{2\pi}\int_0^t G_x(\tau) d\tau \quad \text{Eq. 2.10}$$

$$k_y(t) = \frac{\gamma}{2\pi}\int_0^t G_y(\tau) d\tau \quad \text{Eq. 2.11}$$

$$k_z(t) = \frac{\gamma}{2\pi}\int_0^t G_z(\tau) d\tau \quad \text{Eq. 2.12}$$

and the final form of the signal equation becomes:

$$s(t) = \int_x \int_y \int_z m_0(x,y,z)\, e^{-i2\pi\,[\,k_x(t)\,x + k_y(t)\,y + k_z(t)\,z\,]}\, dx\, dy\, dz. \quad \text{Eq. 213}$$

The signal recorded from the receiver coil $s(t) = M(\,k_x(t),\, k_y(t),\, k_z(t)\,)$, is a 3D Fourier Transform (FT) with spatial frequency variables $k_x(t)$, $k_y(t)$ and $k_z(t)$. This 3D FT space spanned by (k_x, k_y, k_z) is often called k-space.

In MRSI, chemical shift is included in the signal equation:

$$s(t) = \int_x \int_y \int_z \int_f m_0(x,y,z)\, e^{-i2\pi\,[\,k_x(t)\,x + k_y(t)\,y + k_z(t)\,z]}\, e^{-i2\pi f t}\; df\, dx\, dy\, dz. \qquad \text{Eq. 2.14}$$

Variable k_f is defined as $k_f = t$ and:

$$M(k_x, k_y, k_z, k_f) = \int_x \int_y \int_z \int_f m_0(x,y,z)\, e^{-i2\pi\,[\,k_x(t)\,x + k_y(t)\,y + k_z(t)\,z]}\, e^{-i2\pi k_f f}\; df\, dx\, dy\, dz. \qquad \text{Eq. 2.15}$$

The signal recorded from the receiver coil $s(t) = M(\,k_x(t),\, k_y(t),\, k_z(t),\, k_f)$ is now a 4D FT, where the FID is collected along $k_f = t$ as (k_x, k_y, k_z) space is traversed. Different MRSI methods travel in k-space along different trajectories and the following sections give a brief introduction to three MRSI techniques.

2.3.2 Conventional Phase Encoded MRSI

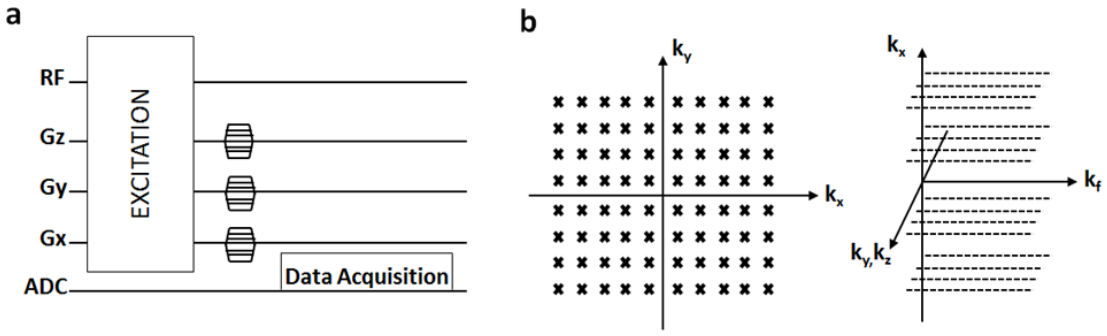

Figure 2-12: (a) Pulse sequence diagram of phase-encoded MRSI scheme (b) k-space trajectory

In conventional phase encoded MRSI, (k_x, k_y, k_z) space is phase-encoded by incrementing linear G_x G_y and G_z gradients in a step wise fashion [43-45]. Figure 2-12 shows a typical phase-encoded MRSI pulse sequence for a single repetition time (TR) and its associated k-space trajectory. After the excitation phase, the G_x G_y or G_z gradients are applied to travel to a particular (k_x, k_y, k_z) point in k-space. After the spatial encoding step, spectral data is acquired without the application of any gradients. The spins are allowed to relax back to equilibrium state before the process is repeated in the next TR. Only one FID is acquired in each TR, so filling up a k_x, k_y, k_z spatial matrix of 16 x 16 x 16 = 4096 points will require a total time of 4096 x TR s. Assuming a TR of 2s for sufficient relaxation to equilibrium, a conventional phase-encoded MRSI with 16 x 16 x 16 spatial points will take about 2h 16min to perform, which is prohibitive for in-vivo applications.

The sampling rate while spectral data is acquired is on the order of ~μs, leading to a spectral bandwidth ~MHz. However at 3.0T, the spectral bandwidth spanned by resonances from brain metabolites is only about 800Hz, requiring a sampling rate of just 1.25ms. This observation motivates the development of more efficient spatial encoding schemes such as spiral spectroscopic imaging and echo-planar spectroscopic imaging (EPSI).

2.3.3 Echo-Planar Spectroscopic Imaging

One can observe that within a sampling rate of 1.25ms necessary for a spectral bandwidth of around 800Hz at 3.0T, more than one (k_x, k_y, k_z) point can be sampled. To traverse k-space during data acquisition, magnetic gradients are switched on during readout. In EPSI [46, 47], rapidly switching frequency-encoding gradients are turned on during data acquisition to move back and forth in k_x or k_y as spectral data is collected.

k_y or k_x and k_z remains phase-encoded. Figure 2-13a shows the switching gradients in G_y and Figure 2-13b shows the corresponding back-and-forth traversal in k_y.

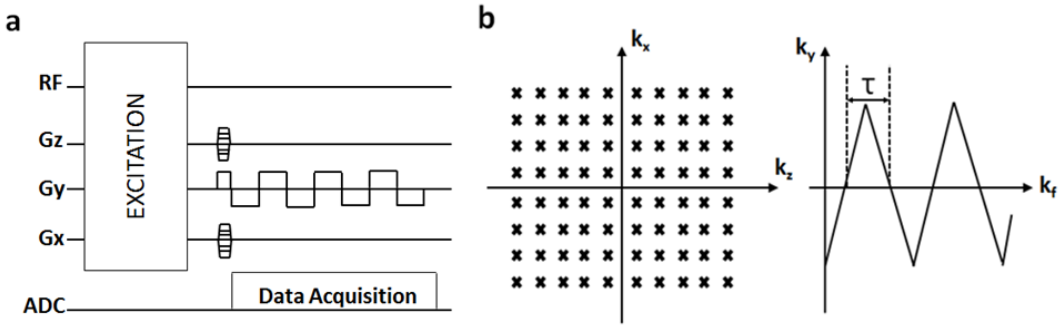

Figure 2-13: (a) Pulse sequence diagram of EPSI scheme (b) k-space trajectory

Subsequent k_f samples for the same (k_x, k_y, k_z) point cannot be separated by more than 1.25ms in order to satisfy spectral bandwidth requirements, i.e. $\tau < 1.25$ms. Assuming that the necessary k_y extent can be traversed in $\tau < 1.25$ms, the total time required to fill up a spatial matrix of 16 x 16 x 16 points is now 256 x TR s. Field inhomogeneities and imperfect gradient switching lead to an asymmetrical zigzag trajectory and aliasing artifacts. Separate processing of "odd" and "even" echoes removes these artifacts but increases the spectral bandwidth requirement by two [47]. The fast acquisition of 2D MRSI data with spatial resolution in x and y was demonstrated with a minimum scan time of 64 seconds for 1cc voxel size in a 32 x 32 spatial matrix and field of view (FOV) = 26cm x 26cm at 3.0T [48].

2.3.4 Spiral Spectroscopic Imaging

In EPSI, data in a spatial and spectral dimension are collected simultaneously for fast traversal of k-space. Spiral SI [49] takes this principle a step further by simultaneously collecting spectral data in two spatial dimensions. In Figure 2-14, spiral gradient waveforms applied along x and y trace out a spiral trajectory in k_y and

k_x while k_z remains phase-encoded. In order to meet spectral bandwidth requirements of 800Hz at 3.0T, the time τ between k_f samples for the same (k_x, k_y, k_z) point must be less than or equal to 1.25ms. If the entire necessary k_y , k_x extent can be traversed within τ < 1.25ms, the total time required to fill up a spatial matrix of 16 x 16 x 16 spatial matrix is just 16 x TR s.

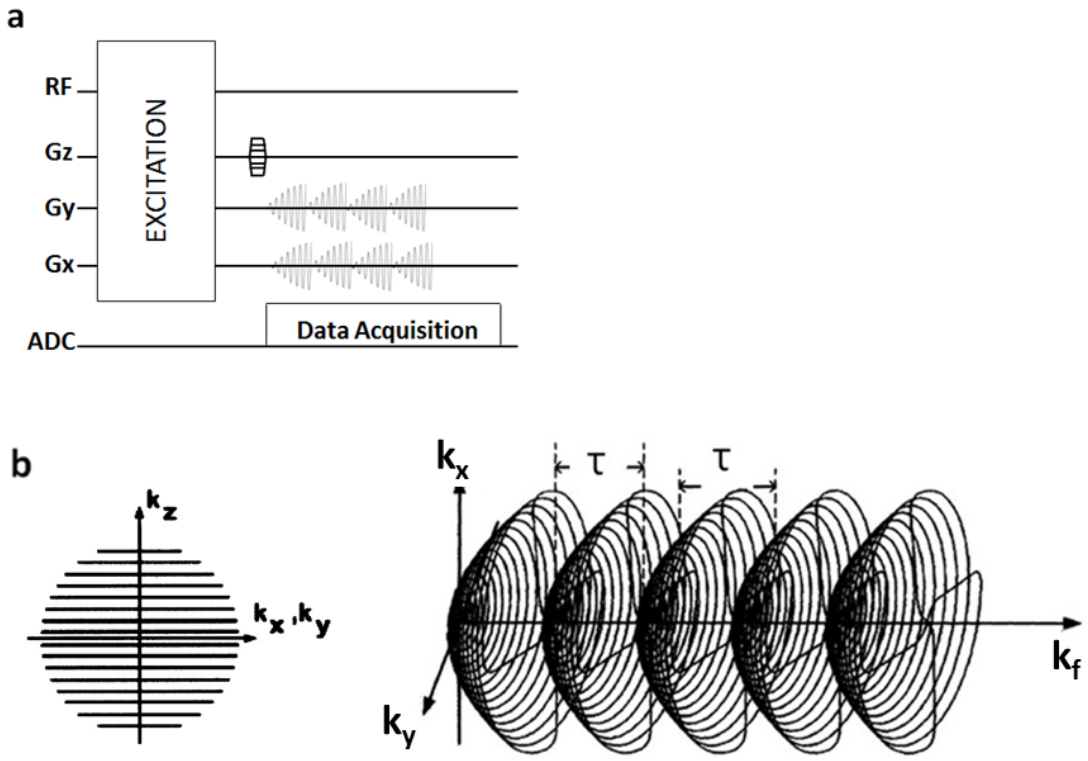

Figure 2-14: (a) Pulse sequence diagram of a spiral SI scheme (b) k-space trajectory

The spatial FOV of the adult human brain is about 20cm and it is impossible to traverse the entire k_y , k_x extent in 1.25ms with clinical gradient hardware for this FOV. Assuming that the entire k_y , k_x space extent can only be traversed in τ = 2.5ms, additional spiral lobes can be interleaved in the k_f dimension by shifting the same spiral encoding to occur 1.25ms later during the readout acquisition of another TR. In this way, every (k_x, k_y) point is temporally spaced 1.25ms apart and the

spectral bandwidth requirement is met. These interleaved spiral lobes are known as temporal interleaves. Note that temporal interleaving requires the spiral lobes to be an integer multiple of the minimum sampling rate, in this case 1.25ms.

It is also possible to divide the desired k-space trajectory into sparser spiral trajectories that takes less time to traverse. Each of these sparser trajectories is then played again in another TR. These trajectories are known as angular interleaves. If data collected from these sparse spiral trajectories were used individually, each data set will produce a spatially aliased image due to violation of the Nyquist requirement.

With both angular and temporal interleaves, fast acquisition of 2D MRSI data with spatial resolution in x and y is possible with a minimum scan time of 12 seconds (N_{avg} =1) for 1.1cc voxel size in and field of view (FOV) = 20cm x 20cm at 3.0T [50].

Spiral encoding MRSI efficiently encodes the spatial dimensions in spectroscopic imaging, and is amenable to combination with 2D MRS for reasonable scan times in in-vivo applications. All spectroscopic imaging in this thesis is implemented with spiral encoding.

2.4 2D MRS with Spectroscopic Imaging

Fast spatial encoding in MRSI enables the integration of 2D MRS techniques so that a 2D spectrum can be obtained for each voxel in the entire volume of interest within reasonable scan times.

EPSI was combined with COSY at 3.0T to implement a spectroscopic imaging sequence known as EP-COSI [51] for applications to in-vivo human calf studies within a minimum scan time of 20-34min. EP-COSI has also been applied to prostate [52] and brain studies [53]. A constant time variant of COSY, CT-COSY was also implemented with EPSI encoding at 4.7T for in-vivo rat brain experiments with a minimum scan

time of 17min for a voxel size of 0.045cc [54], Timing parameters of this CT-COSY implementation were optimized for the detection of myo-Inositol (mI) and taurine (Tau).

Spiral encoding has been implemented at 3.0T with the 17-step CTPRESS to achieve a voxel size of 4.5cc in vivo, within a minimum scan time ($N_{avg} = 1$) of 1:16min using a quadrature birdcage coil [42]. Four averages were taken in this implementation for increased SNR and the total scan time was 4:40 min. In another study, spiral k-space trajectories were also used to speed up acquisitions of 2D JPRESS spectroscopic imaging data in-vivo at 3.0T within scan times of 17min [55]. This dissertation aims to extend further applications of CT-PRESS implemented with spiral encoding for fast 2D MRS imaging experiments.

Chapter 3

Detection of Cortical Metabolites with Lipid Artifact Suppression in High-Resolution CT-PRESS

Multi-element receive coil arrays such as the 32-channel coil arrays offer significant SNR gains over birdcage coils [56], which can be traded for faster scans or improved spatial resolution. As shown in Figure 3-1, much of the SNR increase is in the cortical region near the skull. However, measurements in the changes of cortical metabolite levels, e.g. glutamate (Glu) and glutamine (Gln), in these regions are complicated by the spatial proximity of the cortex to the subcutaneous lipid layer. Despite the spatial separation between brain and skull, ringing artifacts from the lipid signals of the subcutaneous layer contaminate metabolite spectra within the brain. Methods such as outer-volume suppression (OVS) [21-24] and inversion-recovery [25-27] effectively suppress the lipid signals but must trade off outer cortical brain metabolite signals. In the work presented in this chapter, a recent lipid suppression technique [57]

that exploits the approximate orthogonality between lipid and metabolite spectra was combined with a high-spatial-resolution Constant-Time Point Resolved Spectroscopy (CT-PRESS) acquisition implemented with spiral encoding. Signals from cortical metabolites were successfully recovered in a high resolution 1.11c in vivo CTPRESS experiment with a total scan-time of 3:32min ($N_{avg} = 1$).

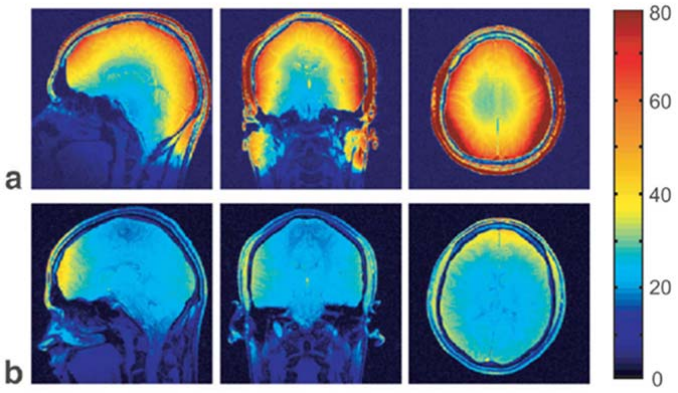

Figure 3-1 SNR maps obtained from gradient echo scans for (a) a 32-channel coil and (b) a 8-channel coil (courtesy of LL Wald). Greatest SNR increase is in the brain tissue region near the skull.

3.1 Spiral Encoded 17-Step CT-PRESS Pulse Sequence

Figure 3-2 shows the implemented pulse sequence at 3.0T for the 17-step CT-PRESS experiment with Water suppression Enhanced through T1 effects (WET) and a PRESS module to excite a selected volume. PRESS was applied on a field of view (FOV) of 20cm x 20m and slice thickness of 1cm. The bandwidth for water suppression was 50Hz. The last 180° pulse of the PRESS-box was shifted in increments of $\Delta t_1/2 =$ 6.4ms to give a spectral bandwidth of 78.125Hz in f_1, while the bandwidth in the f_2 dimension was 1200 Hz. Echo time (TE) ranged from 48.6ms to 253.4ms for an average TE of 151ms as reported in [42] for optimal SNR of Glu and myo-inositol (mI). The full axial slice was excited without localization within the brain and no additional RF

pulses were applied for lipid suppression. Data was acquired immediately after the spoiler gradient pulse of the last 180° pulse, using spiral trajectories with two angular and three temporal interleaves for k-space traversal. This resulted in a nominal voxel size of 1.05cm x 1.05cm x 1cm = 1.11cc. Together with four preparatory scans to bring the system to steady state, the minimum scan time for this acquisition was 3:32 min.

Data was gridded in k_x-k_y space on a 2X grid using a Kaiser-Bessel kernel for convolution, and then apodized in t_1-t_2 space with a 2D tapered-cosine function. A phase term linear with the t_1 step was applied to correct for the collection of data immediately after the last spoiler gradient pulse. Due to the eight-fold undersampling, 2D spectra were unwrapped in f_1 to obtain the 2D CTPRESS spectra. Decoupled diagonal spectra from the 2D CTPRESS experiment were obtained after lipid artifact minimization by integrating the unwrapped magnitude spectra along f2 within ±13Hz along the 2D spectrum diagonal.

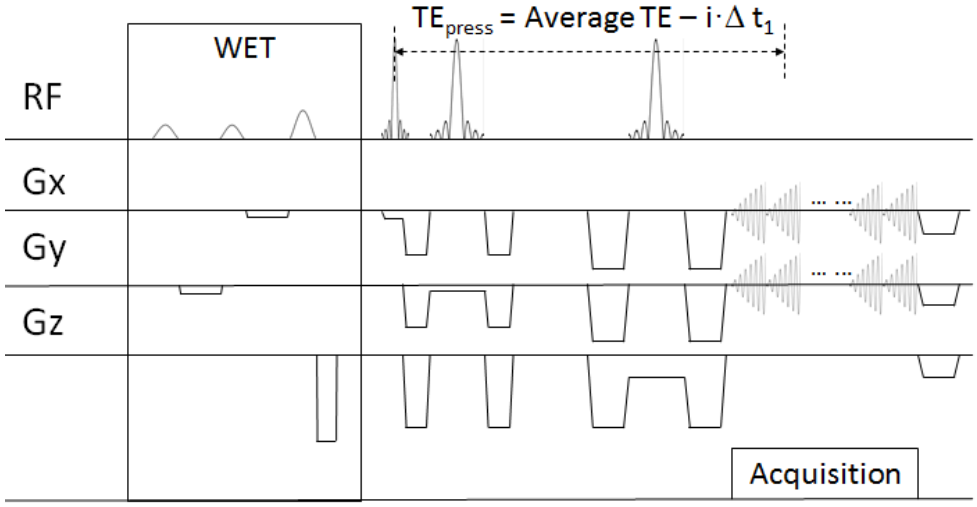

Figure 3-2: Scheme of the CT-PRESS experiment implemented with spiral encoding. WET was used for water suppression. The last 180° pulse of the PRESS module was shifted in increments of $\Delta t_1/2$ for encoding J-coupling and chemical shift information. No OVS module for lipid suppression was applied.

3.2 Lipid Minimization Algorithm

Spectral data was normalized across the 17 t_1 steps and the entire FOV. For each t_1 step, lipid signals within the brain were suppressed by iteratively minimizing the cost function

$$\|\mathbf{F}\boldsymbol{x} - \boldsymbol{y}\|_2^2 + \lambda \sum_{i \in \mathbf{M}_{brain}} \|\mathbf{L}^{\mathbf{H}}\, \boldsymbol{x}_i\|_1 \ , \qquad \text{Eq. 3.1}$$

where $\mathbf{x}$ is the recovered spectral data with minimal lipid contamination within the brain, $\mathbf{y}$ is the data in the k_x-k_y-t_2 dimension and $\mathbf{M}_{brain}$ is a binary mask of the brain-only region in the FOV. $\mathbf{L}$ is a lipid-basis matrix from the lipid-only region of the FOV, formed using the collected spectral data in the x-y-f_2 dimension and spectrally masked to exclude water signal. $\mathbf{F}$ is the Fourier Transform operator and λ is a regularization parameter. While the first term in the cost function maintains consistency between the measured data and the recovered metabolite signals, the second term ensures minimal lipid signals within the brain. The lipid signal penalty term in Eq.3.1 penalizes for overlap of the metabolite spectra with spectra from all lipid-only voxels. This is because lipid signal artifacts within the brain tissue arise from side-lobe ringing of the impulse response and are estimated to be a linear combination of lipid spectra from all voxels in the subcutaneous layer. We used the value of $\lambda = 0.1$ for maximal lipid artifact reduction. The optimization was solved using the conjugate gradient algorithm and took approximately 40min on a 12-core 64bit 3.07GHz Linux machine.

3.3 In-Vivo Trials

MR structural imaging and 2D MR spectroscopic imaging were done on a 3.0T MRI scanner (Siemens AG, Erlangen, Germany) using a detunable birdcage coil for excitation and a 32-channel coil array for signal reception. Structural images were obtained with MP-RAGE to aid in placing the FOV and prescribing the volume of

interest, and post-processed with the brain extraction tool from the FMRIB Software Library (FSL) [11-13].

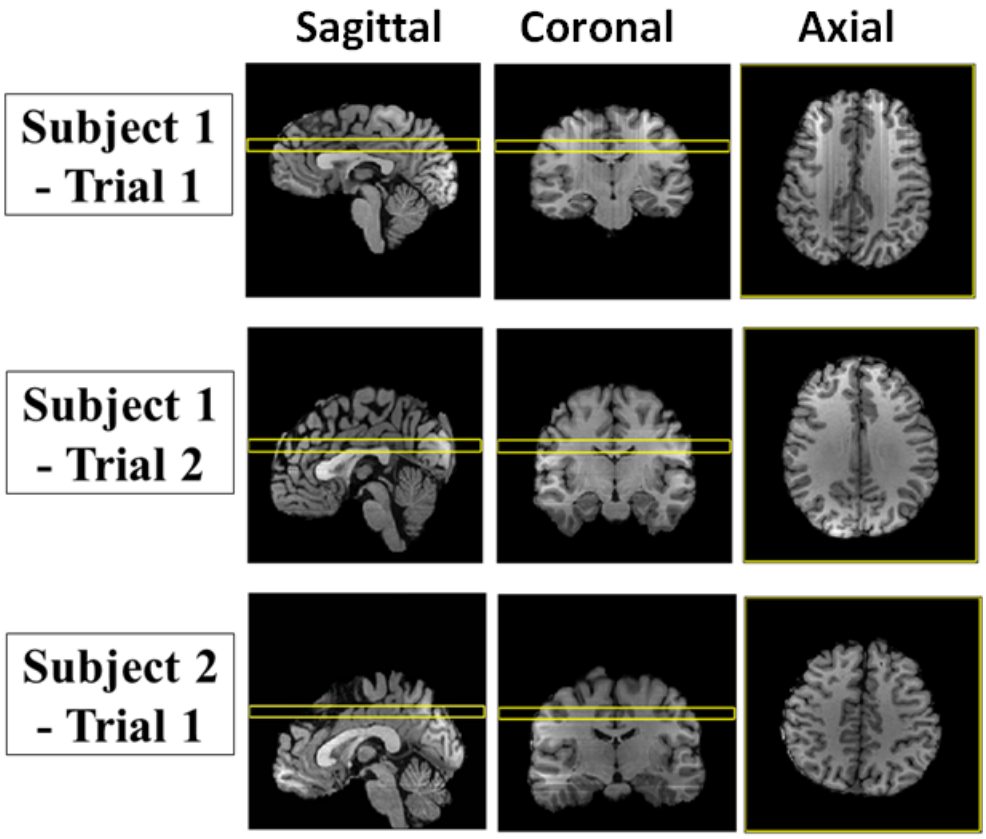

Figure 3-3: Anatomical MP-RAGE of Subject 1 – 1st trial, Subject 1 – 2nd trial and Subject 2 with prescribed slice overlay in sagittal, coronal and axial view. Images are obtained after brain extraction with FSL.

An automatic shim routine using first- and second- order shimming followed by final manual shimming adjustments were done before the 17-step CT-PRESS data was acquired. One average was taken (Navg = 1) for a total scan time of 3:32min. Under an institutional review board approved protocol, two subjects (Subject 1 and Subject 2) were recruited for participation. To demonstrate reproducibility, the same protocol was repeated after a span of four weeks on Subject 1. Figure 3-3 shows the anatomical MP-

RAGE after post-processing with FSL, with the prescribed slice overlay for each of the three trials.

3.3.1 Validation of Lipid Artifact Minimization

For validation of the lipid minimization algorithm, the same 17-step CT-PRESS experiment was repeated on Subject 1 and compared with a 17-step CT-PRESS experiment with identical acquisition parameters, except with OVS bands applied, a different location for the FOV = 20cm x 20cm, and a selected volume of interest of 50cm x 50cm. Four averages were taken for increased SNR and the total scan time for each of the two experiments was 13:44min. Figure 3-4a and b show the FOV and PRESS box locations of the experiments without OVS and with OVS pulses respectively. Spectra from voxels near the vicinity of the skull are compared. These voxels are located in both volumes of interest with either lipid suppression method applied.

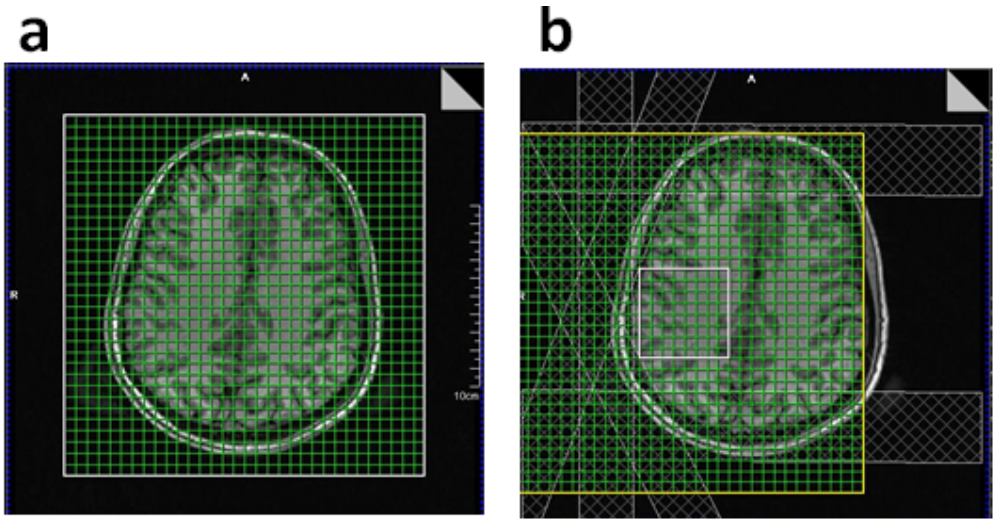

Figure 3-4: (a) Anatomical image with prescribed FOV and volume of interest in white rectangle. The entire axial slice was excited and no additional RF pulses were used for excitation. (b) Anatomical image with prescribed FOV and selected volume of interest (in white rectangle) overlaid. OVS bands are placed around the brain tissue in the excited volume.

3.4 Results

Figure 3-5 shows CSI images with and without lipid suppression, obtained by summing over the range of lipid resonance frequencies in the diagonal decoupled spectra from 0.1ppm to 1.9ppm. As shown, lipid signal in the brain is considerably reduced after the lipid minimization algorithm is applied.

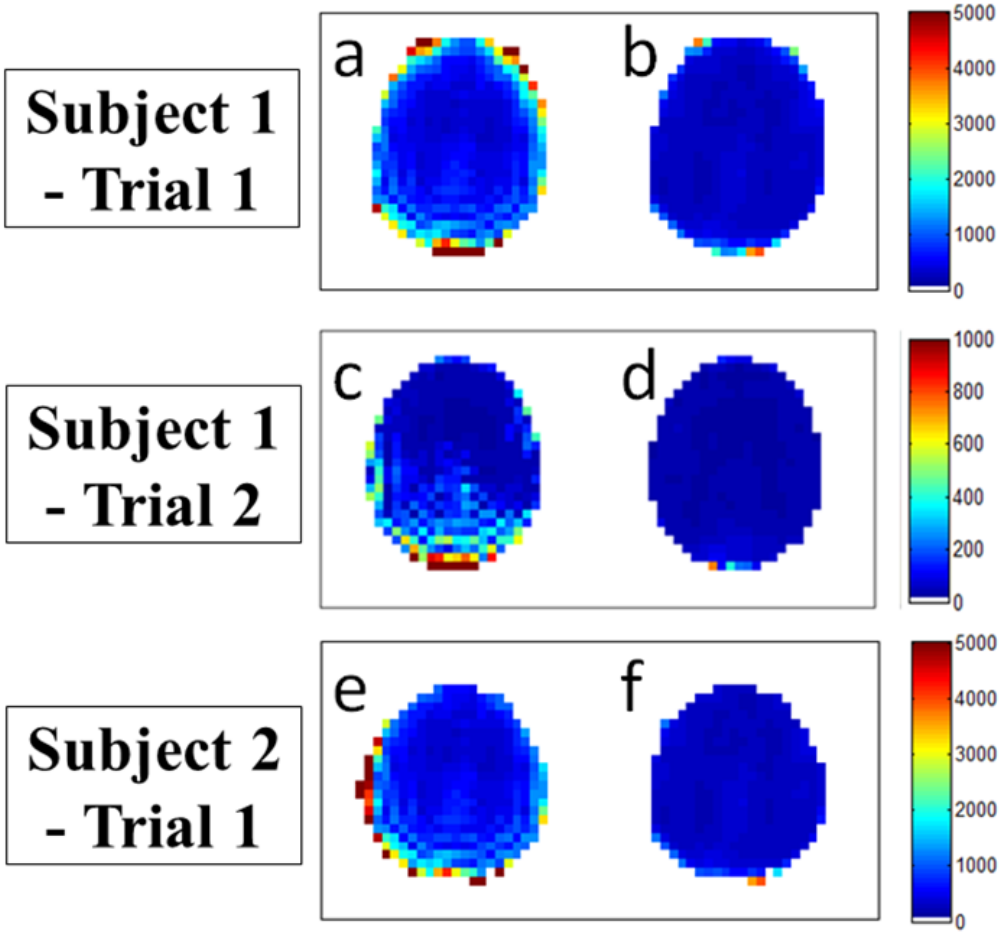

Figure 3-5: Projections in linear scale taken by summing over the range of lipid resonance frequencies in the diagonal decoupled spectra (a,c,e) before lipid artifact suppression algorithm is applied and (b,d,f) after lipid suppression algorithm is applied for the three in-vivo trials of (I) Subject 1 – 1st trial (II) Subject 1 – 2nd trial (III) Subject 2

Figure 3-6a and b show the diagonal spectrum obtained before application of the proposed lipid suppression method in blue, and the spectrum after application of the lipid minimization algorithm in black. Without lipid artifact reduction with the proposed algorithm, Figure 3-6a shows that the large lipid signal overcomes the metabolites signal, especially between 1ppm-2ppm and 2.2ppm-2.8ppm. Figure 3-6b is scaled for a better presentation of the metabolites resonances and figures presented henceforth will be scaled as such.

A map of the diagonal spectra for cortical voxels in the vicinity of the skull from the 2nd trial of Subject 1 are displayed in Figure 3-7 demonstrating the successful suppression of lipid artifacts in all the voxels and the recovery of the dominant NAA peak at 2.0ppm which would have overlapped with the lipid signals.

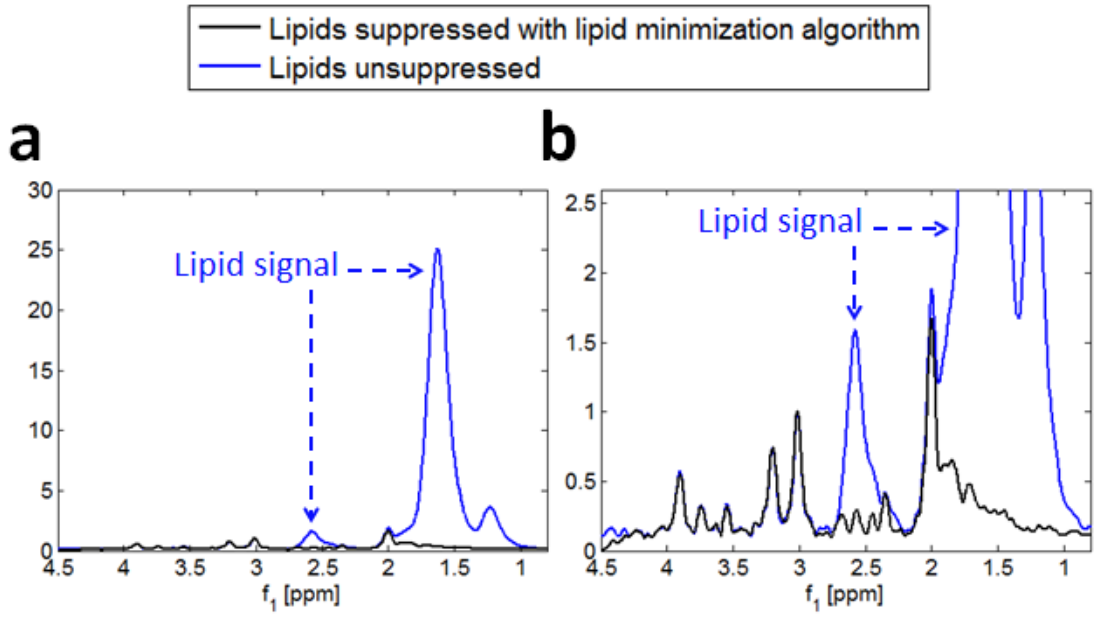

Figure 3-6: Diagonal spectrum of a voxel near the skull from Subject 1-2nd trial. All spectra are normalized to the amplitude of the creatine (Cr) signal at 3.0ppm. (a) Spectrum showing substantial lipid contamination that obscures metabolite signals. (b) Spectrum zoomed in so that the metabolites may be better presented.

Figure 3-8, Figure 3-9, Figure 3-10 show the unwrapped contour 2D spectra and corresponding diagonal spectra for five specific voxels A, B, C, D and E in the brain tissue. Voxels A, B, C and D are near the skull while voxel E is approximately at the middle of the brain tissue. Baseline fluctuations due to macromolecular contamination are minimal in the diagonal spectra because of the long average TE used. Lipid signal is successfully suppressed so that the dominant peak of NAA at 2ppm is recovered. The peaks of Glu, NAA and Gln between 2.25ppm and 2.50ppm and 3.50-3.80 ppm, which would otherwise be obscured by spectral lipid artifacts, are also successfully recovered. Peaks of Glu, NAA and Gln between 2.25ppm and 2.50ppm and 3.50-3.80 ppm were not present in the spectra for voxel 'E'.

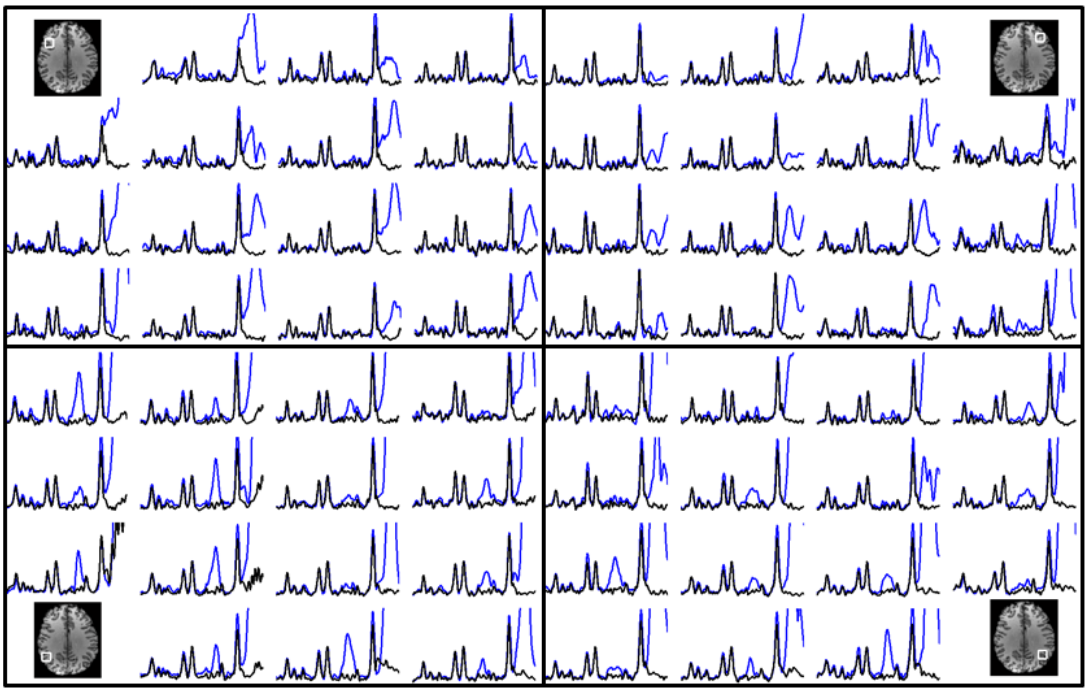

Figure 3-7: Map of diagonal decoupled spectra from 2nd trial of Subject 1 at four regions of brain tissue near the subcutaneous layer. Black lines are spectra obtained after lipid suppression algorithm was applied; Blue lines are spectra obtained before lipid suppression algorithm was applied.

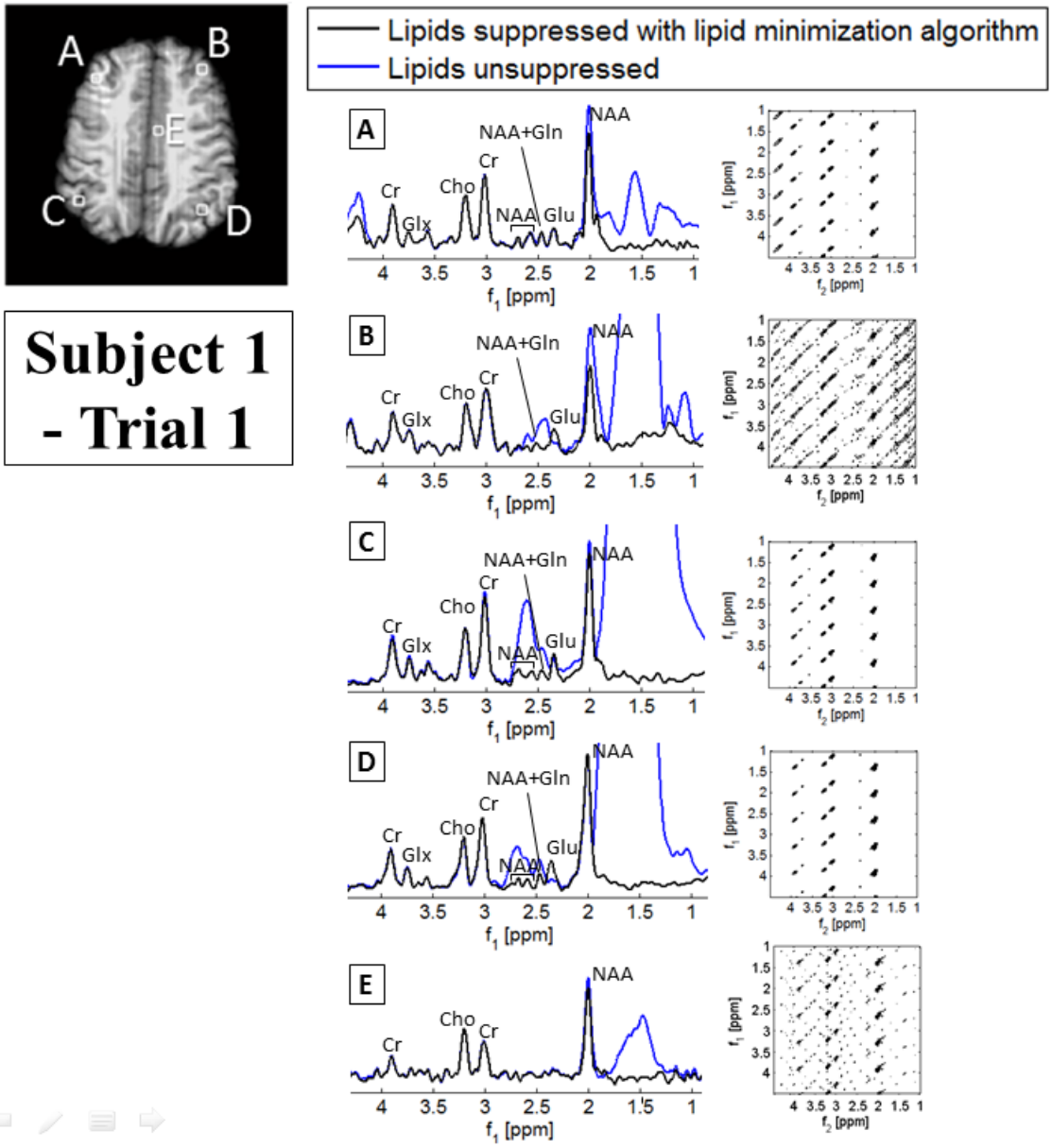

Figure 3-8: Corresponding diagonal decoupled spectra and 2D unwrapped contour plots for Subject 1- 1st trial, for five CSI voxels highlighted at locations 'A', 'B', 'C', 'D' and 'E'. Voxels at 'A'-'D' are near the skull while voxel at 'E' is near the middle of the brain

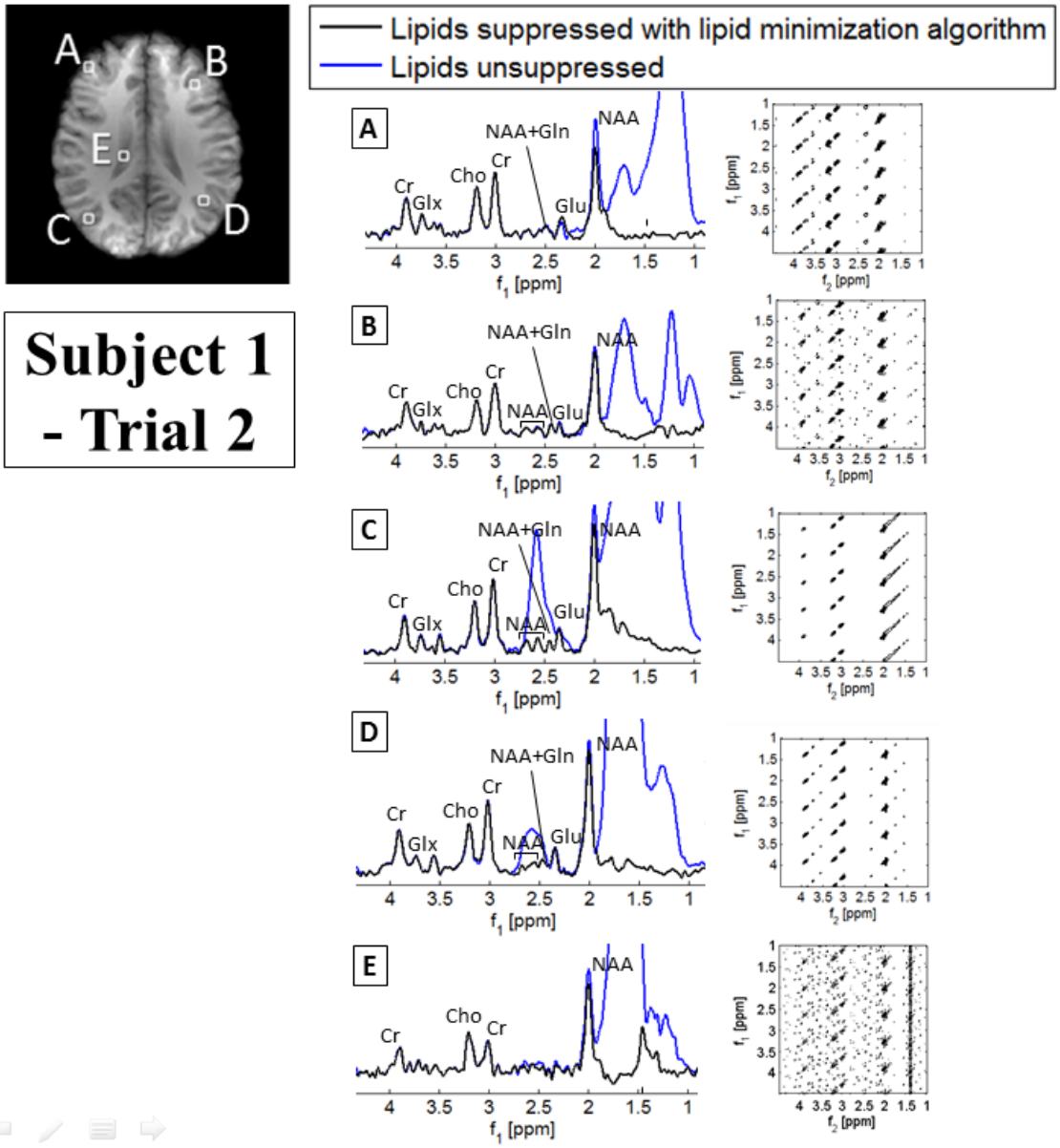

Figure 3-9: Corresponding diagonal decoupled spectra and 2D unwrapped contour plots for Subject 1- 2nd trial, for five CSI voxels highlighted at locations 'A', 'B', 'C', 'D' and 'E'. Voxels at 'A'-'D' are near the skull while voxel at 'E' is near the middle of the brain

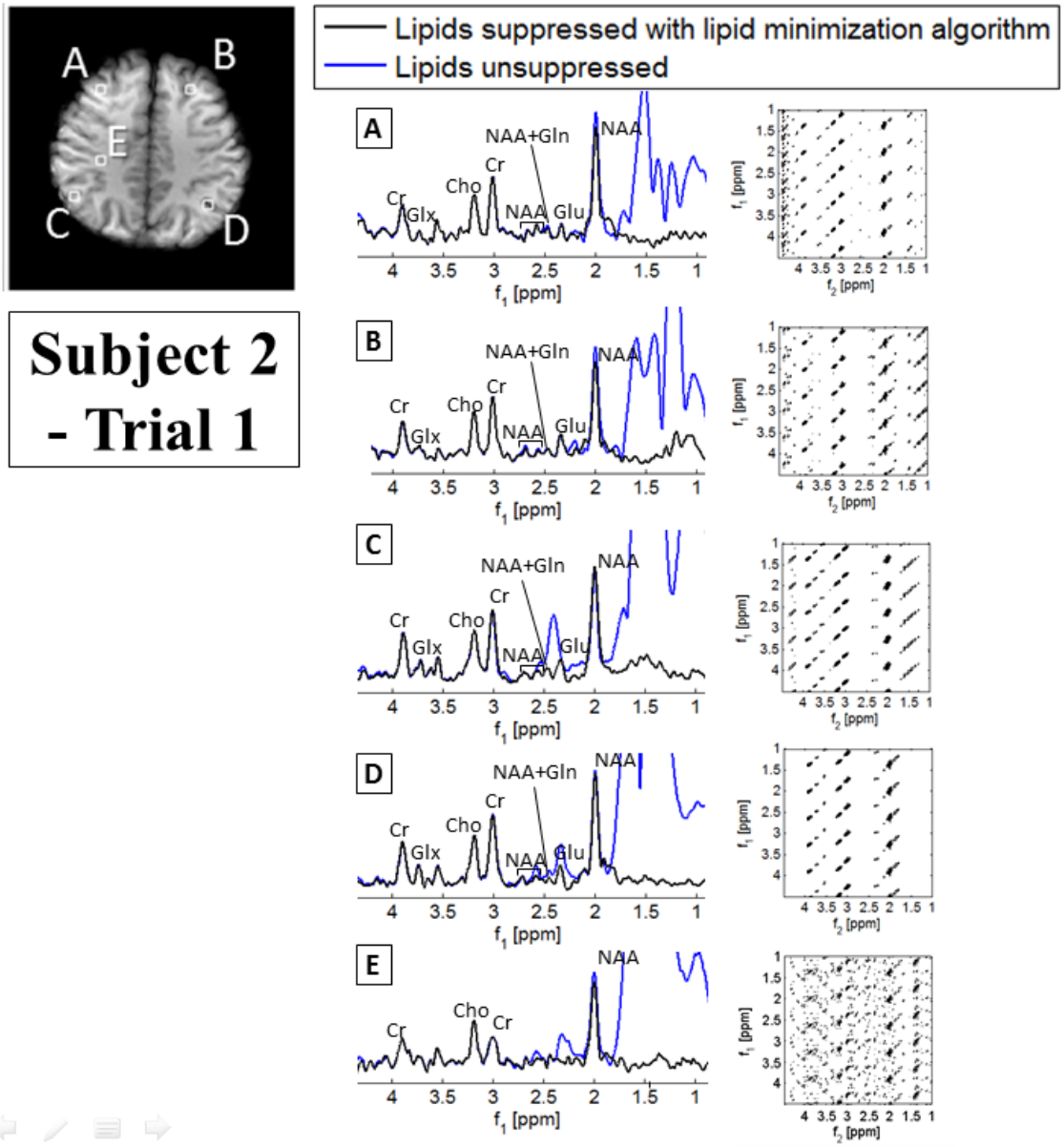

Figure 3-10: Corresponding diagonal decoupled spectra and 2D unwrapped contour plots for Subject 2- 1st trial, for five CSI voxels highlighted at locations 'A', 'B', 'C', 'D' and 'E'. Voxels at 'A'-'D' are near the skull while voxel at 'E' is near the middle of the brain

3.4.1 Validation of Lipid Artifact Minimization

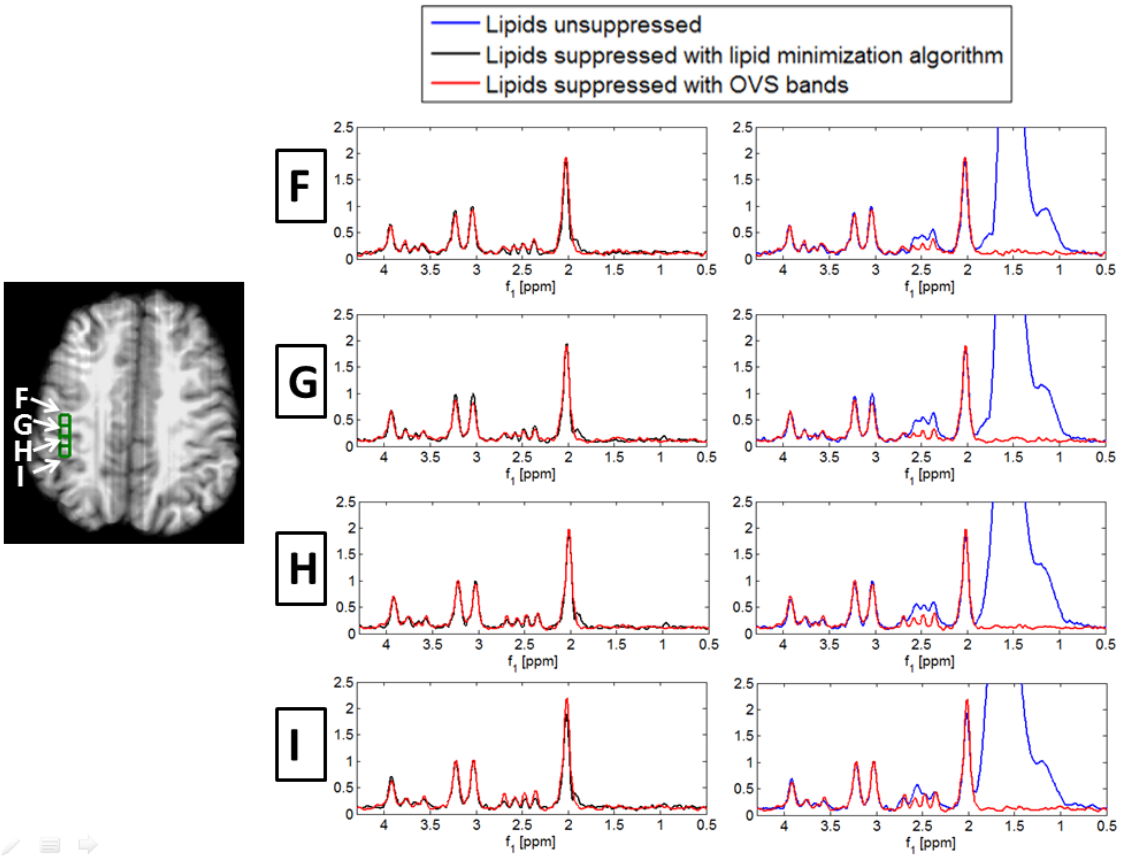

Figure 3-11: Diagonal spectra from voxels at locations indicated by 'F' 'G', 'H' and I in the anatomical image. Lipid artifact minimization using proposed algorithm successfully reduces lipid artifacts between 2.2ppm and 2.8ppm. Spectra processed with lipid minimization algorithm are compared with spectra obtained with lipid suppression using OVS bands and shows good agreement.

Figure 3-11 shows the diagonal spectra from four particular voxel locations 'F', 'G' and 'H' and 'I'. Lipid contamination obscuring Glu, NAA and Gln signal in the 2.2ppm-2.8ppm frequency range is completely removed by the proposed lipid minimization algorithm. Diagonal spectra obtained from applying the lipid minimization algorithm agrees with the spectra obtained with OVS bands applied. This demonstrates the validity of the lipid minimization algorithm.

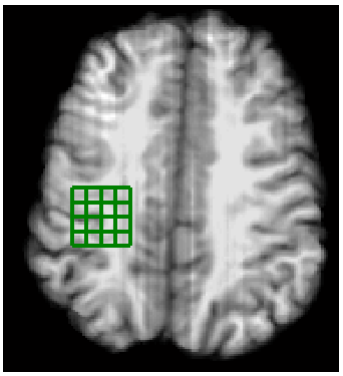

Figure 3-12: The 4 x 4 volume for which RMSE is calculated for the spectra obtained with the proposed lipid minimization algorithm and with OVS bands applied. Mean RMSE values obtained by averaging across the 16 voxels.

$$\text{RMSE} = \sqrt{\frac{\sum_{f=f_a}^{f=f_b}\left(x_1(f)-x_2(f)\right)^2}{f_b-f_a}} \qquad \text{Eq. 3.2}$$

To get a quantitative measure of the agreement between the two lipid suppression methods, the root mean square error (RMSE) between the two spectra is calculated using Eq. 3.2. f_a-f_b represents the frequency range for which the RMSE is calculated. $x_1(f)$ and $x_2(f)$ are the two spectra that are being compared.

RMSE is determined for all the voxels in the 4 x 4 volume shown in Figure 3-12 and for the frequency ranges 1.8-4.1ppm (ALL), 1.9-2.2ppm (NAA), 2.2-2.8ppm (NAA/Glu/Gln), 3-3.12ppm (Cr) and 3.15-3.3ppm (Cho). Mean RMSE values are summarized in Figure 3-13 and compared to that for the range between 0-0.75ppm, where we assume the absence of metabolite signal and consequently, only noise is present.

The mean RMSE for the four peaks of metabolites NAA, Glu and Gln in the 2.2-2.8ppm range is at 0.7 ± 0.2, which is greater than the mean value of 0.5 ± 0.1 attributed to noise. This indicates that while we have eliminated enough fat to detect these four peaks, the difference between the two curves is not completely accounted for

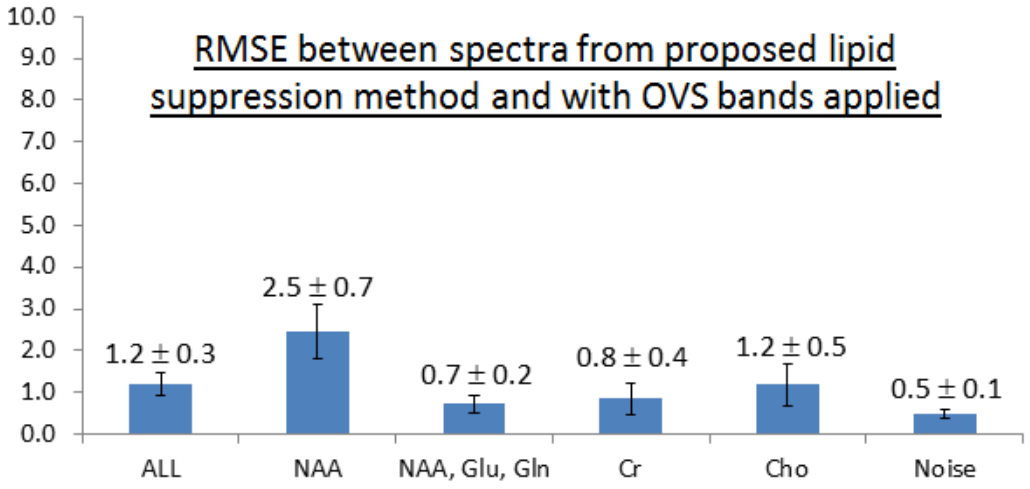

Figure 3-13: Mean RMSE values between spectra obtained with the proposed lipid minimization algorithm and with OVS bands applied for different frequency ranges

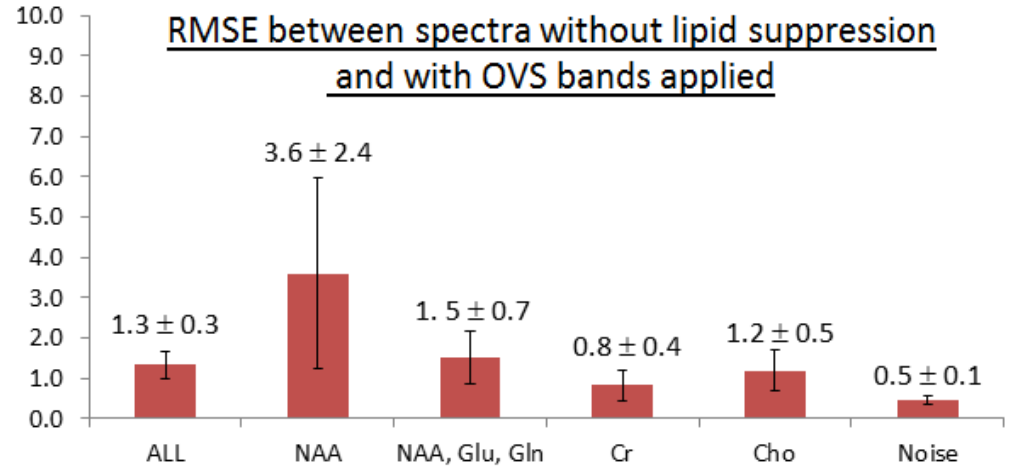

Figure 3-14: Mean RMSE values between spectra obtained with the proposed lipid minimization algorithm and with OVS bands applied for different frequency ranges

by noise, and is likely due to incomplete fat suppression for voxels near the skull. The mean RMSE for the NAA peak in the 1.9-2.2ppm region is at 2.5 ± 0.7, higher than that for the peaks between 2.2-2.8ppm. This is likely attributed to the reduced effectiveness of the proposed lipid suppression method in this region, as the resonant frequency is closer to that of the lipid signals.

Although the proposed method does not achieve fat suppression as well as with OVS bands applied, lipids are reduced by a substantial amount so that peaks of NAA, Glu and Gln in the 2.2-2.8ppm manifest as four distinguishable peaks. Figure 3-14 summarizes the RMSE values between two spectra obtained with OVS bands applied and without any lipid suppression. In this case, RMSE values for the NAA, Glu and Gln peaks between 2.2-2.8ppm and for the NAA peak between 1.9-2.2 ppm are substantially higher than that for the proposed lipid minimization algorithm.

3.5 Discussion

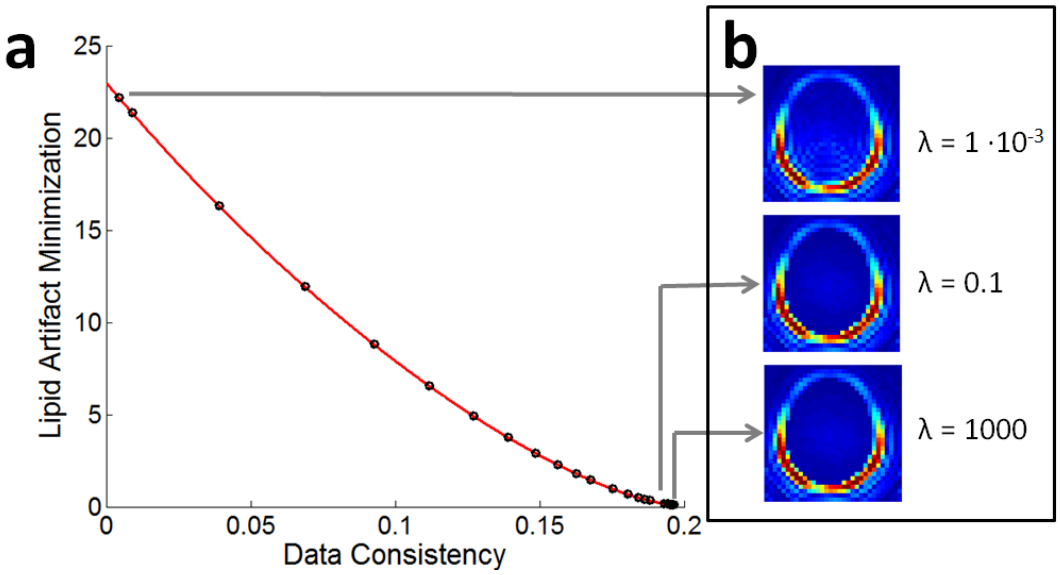

Figure 3-15: (a) L-curve traced by the data consistency and lipid-basis penalty terms as regularization parameter $\boldsymbol{\lambda}$ varies for the 1st t_1 step at TE = 48.6ms (b) Projections over lipid frequencies of the recovered spectral data for selected $\boldsymbol{\lambda}$ values.

The regularization parameter λ determines the trade-off between the first term for data consistency and the second term for lipid artifact minimization. The iterative reconstruction was done for several different regularization parameters where the resulting data consistency term $\|\mathbf{F}\boldsymbol{x} - \boldsymbol{y}\|_2$ and lipid signal penalty term $\sum_{i \in \mathbf{M}_{brain}} \|\mathrm{L}^{\mathrm{H}}\, \boldsymbol{x}_i\|_1$ traced a curve. Figure 3-15a shows this curve for the 2nd trial of

Subject 1 and for the 1st t_1 step at TE = 48.6ms. Figure 3-15b shows the corresponding projections over lipid frequencies of the recovered spectral data x for selected λ values. For lipid artifact suppression, we used the value of $\lambda = 0.1$ where the lipid signal penalty term is close to its minimum. For all 17 t_1 steps, as λ is increased from 0.1 to 1000, the increase in the data consistency term $\|\mathrm{F}x - y\|_2$ ranged from 0.0070 % to 0.5615% and the decrease in the lipid signal term $\sum_{i\in \mathrm{M}_{brain}} \|\mathrm{L}^{\mathrm{H}}\, x_i\|_1$ ranged from 1.05% to 12.48%.

Hence a slightly over-regularized reconstruction is preferable for improved lipid artifact suppression since the data consistency term is relatively insensitive to higher values of λ.

SNR gains from the receive coil arrays in the cortical region of brain tissue near the skull is traded off for a 1.11cc scan in a scan time of 3:24min. For both trials of Subject 1 and the single trial of Subject 2, peaks of Glu, NAA and Gln between 2.25ppm and 2.50ppm and 3.50-380 ppm were recovered in voxels near the skull, demonstrating reproducibility of the 17-step CT-PRESS experiment across subjects. Peaks of Glu, NAA and Gln were not detectable in regions near to the brain center because of insufficient SNR in this region of brain tissue. To recover Glu, NAA and Gln peaks in this region, multiple averages can be taken for increased SNR due to the relatively short scan time of 3:24 min.

For absolute metabolite quantitation based on the homonuclear decoupled spectra, B_o and B_1 field variations and T_2 decay have to be taken into consideration. B_o and B_1 field mapping and correction methods could be done to correct for field variations. Each step of the CT-PRESS experiment was taken at incremental TE values and T_2 values could be determined from the signal intensities at different TE steps.

The availability of multi-channel coils with more elements e.g. 96-channel receive coil arrays [58] allows for the possibility of a greater trade-off for higher resolution and shorter scan time. An immediate extension is to enable 3D spectroscopic imaging by incorporating phase-encoding in k_z space. The corresponding increase in minimum measurement time could be traded off for higher resolution or better SNR.

3.6 Conclusion

A high-resolution 1.11cc CT-PRESS experiment with a total scan time of 3:24min was implemented with spiral encoding at 3.0T and with the 32-channel receive coil. Peaks previously obscured by artifactual lipid signal such as the Glu, NAA and Gln signal between 2.2ppm-2.8ppm were successfully recovered. Lipid suppression with the proposed algorithm was compared with lipid suppression via OVS bands. Diagonal spectra of voxels near the skull reconstructed after lipid suppression by the proposed lipid minimization algorithm was in good agreement with the corresponding spectra obtained with the application of OVS bands. With the increased SNR from the multi-channel receive array, major cortical metabolites of NAA, Cr, Cho and Glu, Gln and mI are successfully imaged near the skull without the use of OVS or inversion recovery for fat suppression.

Chapter 4

Multi-Task Bayesian Compressed Sensing in Sparse 2D Spectroscopy

As mentioned in Chapter 2, Constant-Time Point Resolved Spectroscopy (CT-PRESS) is a homonuclear decoupling method that encodes J-coupling information within metabolite molecules in a 2D frequency plane (f_1-f_2), and has been shown to successfully detect coupled resonances such as glutamate (Glu) and glutamine (Gln) at the expense of increased total scan time in a 129-step CT-PRESS experiment [40, 41]. A 17-step CT-PRESS experiment was implemented by Mayer et al [42] considering that all of the signals from a CT-PRESS experiment lie close to the diagonal in the 2D frequency plane, and therefore uniform under-sampling in f_1 is possible without aliased signal overlap. Exploration of further under-sampling in 2D spectroscopy via compressed sensing appears promising as 2D spectra are naturally sparse and data sampling along the t_1 encoding direction readily accommodates flexible sampling patterns.

Metabolite spectra simulated with a software package SPINEVOLUTION [59] were included as prior spectral information for regularization during the reconstruction

of under-sampled 2D spectra with Multi-Task Bayesian Compressed Sensing (MT-Bayesian CS) [60]. The performance of MT-Bayesian CS was evaluated via numerical simulation and in-vivo application, and compared with Single Task Bayesian Compressed Sensing (ST-Bayesian CS) [61], a solution via an l_1-regularized formulation [62] and least squares fitting with individual simulated metabolite spectra. Linear Combination of Model Spectra LCModel [63] incorporates phase, chemical shift and line-width variations and is widely used for spectral fitting and accurate quantification of metabolites. The least squares fitting model considered in this chapter is a simplistic model that does not include field variations or differences in relative peak amplitudes among resonances from the same metabolite, but included to demonstrate the robustness of MT-Bayesian CS reconstructions to inaccurate prior spectral information. Since spectroscopy data are intrinsically low SNR, noise modeling parameters for MT-Bayesian CS were also briefly explored for improved reconstruction of under-sampled 2D spectra in CTPRESS.

4.1 Introduction: Compressed Sensing

Different MRI images exhibit sparsity in different transform domains. MRI angiograms provide images of vessels and are largely piece-wise constant. They can be sparsely represented by computing the differences between neighboring voxels, i.e. with the Total-Variation (TV) transform. MRI brain images can be sparsely represented in the wavelet transform domain with little visual loss of information. 1D and 2D MRS data are naturally sparse in the f_1-f_2 domain so that the sparse transform domain is the image domain itself i.e. the identity transform.

It has been proven that it is possible to recover images and data from a small number of randomly sampled k-space measurements with a non-linear reconstruction algorithm [64, 65]. This process is known as compressed sensing (CS). By exploiting the

sparsity of MRI images, compressed sensing has enabled significant reduction in scan time and high acceleration factors in in-vivo experiments.

4.1.1 Random Under-sampling

In conventional MR imaging, K-space has to be sampled frequently enough in order to meet FOV requirements of an MRI image e.g. the brain. If k-space samples are uniformly under-sampled, aliasing will occur due to the violation of the Nyquist criterion. The MRI image will fold onto its replica artifact and be no longer of diagnostic quality.

Random under-sampling of k-space results in incoherent artifacts that behave like additive random noise in a zero-filled image. These artifacts are a result of leakage of energy from non-zero coefficients in image space. One could perform thresholding on the signal to recover high amplitude coefficients, calculate the interference caused by these components and subtract it from the zero-filled image to recover coefficients with smaller amplitude. By iteratively performing this thresholding procedure, even smaller coefficients can be recovered.

In 2D MRS, data along one time dimension t_1 is collected indirectly so that under-sampling along t_1 is straightforward. Thus, under-sampling for the CT-PRESS experiment in this chapter is done along t_1.

4.1.2 Non-Linear Reconstruction

Without prior knowledge that MRI images are sparse in some domain and given a randomly under-sampled set of k-space data, a reasonable approximation for obtaining the MRI image is to obtain a least squares estimate from the data collected in k-space i.e.

$$\hat{\boldsymbol{x}} = \arg\min_{\boldsymbol{x}} \left|\left|\boldsymbol{y} - \mathbf{F}_u \boldsymbol{x}\right|\right|_2^2 \quad \text{Eq. 4.1}$$

where $\mathbf{y}$ is the observed data in k-space, $\mathbf{x}$ is the true image data $\mathbf{F}_u$ is the under-sampled FT operator

In Eq. 4.2, an l_0 norm is included to regularize the reconstruction of the image data $\mathbf{x}$, in order to incorporate the knowledge that the data is sparse in some transfer domain, Φ. In the case of MRS data, Φ is simply the identity transform. Here the l_0 norm $\left|\left|\Phi x\right|\right|_0$ is not a true norm but represents the number of non-zero coefficients in Φx. Eq. 4.2 is a non-convex optimization problem, and in general finding the sparsest solution to this problem is NP-hard.

$$\hat{x} = \arg\min_x \left|\left|y - \mathrm{F}_u x\right|\right|_2^2 + \lambda \left|\left|\Phi x\right|\right|_0 \quad \text{Eq. 4.2}$$

$$\hat{x} = \arg\min_x \left|\left|y - \mathrm{F}_u x\right|\right|_2^2 + \lambda \left|\left|\Phi x\right|\right|_1 \quad \text{Eq. 4.3}$$

So, the optimization problem in Eq 4.2 is instead approximated by Eq 4.3 by replacing the l_0 norm with the l_1 norm. The l_1 norm does not enforce a strict count of non-zero coefficients but nonetheless promotes sparsity. This l_1-regularized formulation has been demonstrated to reconstruct under-sampled 2D MRS EPSI data with good fidelity to the original fully sampled data [66]. The entropy of MRS data was used for regularizing reconstructions from the Maximum Entropy algorithm (MaxEnt), yielding reasonable reconstructions for 2D MRS and MRS data with higher dimensionalities [67-69].

4.2 Introduction: Bayesian Compressed Sensing

The previous section introduced compressed sensing and its approximate solution by an l_1 regularized formulation. This section considers solving the inversion of compressive measurements by Bayesian linear regression analysis, in order to set up a

framework where simulated spectral information can be included to improve the reconstruction of under-sampled 2D CT-PRESS data.

$$\boldsymbol{y} = \mathbf{F}\boldsymbol{x} + \boldsymbol{n} \quad \text{Eq. 4.4}$$

$$p(\boldsymbol{y}|\boldsymbol{x}) = (2\pi\sigma^2)^{-K/2}\ \exp(-\frac{1}{2\sigma^2}\left|\left|\boldsymbol{y} - \mathbf{F}_u\boldsymbol{x}\right|\right|^2) \quad \text{Eq. 4.5}$$

$$p(\boldsymbol{x}) = (\lambda/2)^M \quad \exp(-\lambda \sum_{i=1}^{M} |x_i|) \quad \text{Eq. 4.6}$$

In Eq. 4.4 2D MRS data are modeled as being corrupted by additive white Gaussian noise with variance σ^2, where $\mathbf{y}$ is the observed data in kf_1-kf_2 space, $\mathbf{x}$ is the true spectral data and is a naturally sparse signal, $\mathbf{n}$ is the additive noise and $\mathbf{F}_u$ is the under-sampled FT operator. K measurements are made of $\mathbf{x}$ and this gives us the likelihood model with Gaussian probability density function (pdf) in Eq. 4.5 for observing $\mathbf{y}$ given $\mathbf{x}$. The knowledge that $\mathbf{x}$ is sparse is incorporated with a sparseness promoting prior via the Laplace density function in Eq. 4.6, where M is the number of sparse coefficients in $\mathbf{x}$.

Bayes rule in Eq. 4.7 provides the posterior probability and the maximum a posteriori solution given in Eq. 4.8, which is very similar to the l_1 regularized formulation from Eq. 4.3.

$$p(\boldsymbol{x}|\boldsymbol{y}) = \frac{p(\boldsymbol{y}|\boldsymbol{x})\, p(\boldsymbol{x})}{p(\boldsymbol{y})} \quad \text{Eq. 4.7}$$

$$\boldsymbol{x}_{MAP} = \arg\min_{\boldsymbol{x}} \left|\left|\boldsymbol{y} - \mathbf{F}_u\boldsymbol{x}\right|\right|_2^2 + \ 2\sigma^2\lambda\, ||\boldsymbol{x}||_1 \quad \text{Eq. 4.8}$$

The Laplace density function however is not conjugate to the Gaussian likelihood function and linear regression cannot be performed. Instead the hierarchical prior shown in Eq. 4.9 and 4.10 is used.

$$p(\boldsymbol{x}|\boldsymbol{\alpha}) = \prod_{i=1}^{N} N(w_i|0, {\alpha_i}^{-1}) \quad \text{Eq. 4.9}$$

$$p(\boldsymbol{\alpha}|c,d) = \prod_{i=1}^{N} \Gamma(\alpha_i|c,d) = \prod_{i=1}^{N} \frac{c^d}{\Gamma(c)} {\alpha_i}^{c-1} \exp(-d\alpha_i) \quad \text{Eq. 4.10}$$

The overall prior on x becomes:

$$p(\boldsymbol{x}|c,d) = \prod_{i=1}^{N} \int_0^{\infty} N(x_i|0{\alpha_i}^{-1})\, \Gamma(\alpha_i|c,d)\, d\alpha_i \ . \quad \text{Eq. 4.11}$$

A Gamma prior is also defined on the noise precision $\alpha_0 = \sigma^2$ in Eq. 4.12 and included in the signal prior of Eq. 4.13, so that we can integrate out α_0 analytically when computing the posterior probability and circumvent the need for an initial estimate of σ^2.

$$p(\alpha_0|a,b) = \Gamma(\alpha_0|a,b) = \frac{a^b}{\Gamma(a)} {\alpha_0}^{a-1} \exp(-b\alpha_0) \quad \text{Eq. 4.12}$$

$$p(\boldsymbol{x}|\alpha,\alpha_0) = \prod_{i=1}^{N} N(w_i|0, {\alpha_i}^{-1}, {\alpha_0}^{-1}) \quad \text{Eq. 4.13}$$

The posterior probability for $\mathbf{x}$ can be expressed analytically as a Gaussian pdf with mean $\boldsymbol{\mu}$ and covariance $\boldsymbol{\Sigma}$

$$\boldsymbol{\mu} = \boldsymbol{\Sigma}\, {\mathbf{F}_u}^T \boldsymbol{y} \quad \text{Eq. 4.14}$$

$$\boldsymbol{\Sigma} = (\mathbf{F}_u{}^T \mathbf{F}_u + \mathbf{A})^{-1} \quad \text{Eq. 4.15}$$

where $\mathbf{A} = \text{diag}(\alpha_1, \alpha_2, \ldots \ldots \alpha_N)$. The mean and covariance of the posterior is determined from the point estimates of α via evidence maximization (EM) or type-II maximum likelihood (ML) estimate. The EM process involves finding the point estimates that makes the kf_1-kf_2 space data most likely i.e. the α that maximizes

$$L(\boldsymbol{\alpha}) = \log \int p(\boldsymbol{y}|\mathbf{x}, \alpha_0)\, p(\boldsymbol{x}|\boldsymbol{\alpha}, \alpha_0)\, p(\alpha_0|\mathrm{a}, \mathrm{b}) d\boldsymbol{x}\, d\alpha_0 \qquad \text{Eq. 4.16}$$

4.3 Multi-Task Bayesian Compressed Sensing

Metabolite peak locations are frequently known and can be simulated via software packages such as GAMMA [70] and SPINEVOLUTION [59]. The hierarchical Bayesian model introduced in the previous section can capture the similarities between these simulated spectra and in-vivo spectra, via a shared set of hyper-parameters $\boldsymbol{\alpha}$, common across the simulated and in-vivo spectra. In this setting, a joint Bayesian linear regression can be performed. Since the simulated spectra are fully sampled, their inclusion in the joint Bayesian analysis will help in the estimation of $\boldsymbol{\alpha}$ and subsequently the mean, $\boldsymbol{\mu}$ and covariance, $\boldsymbol{\Sigma}$ corresponding to the under-sampled in-vivo metabolite spectra. The likelihood function and signal priors are shown in Eq. 4.17 and Eq. 4.18 respectively, where i indexes the fully sampled simulated and the under-sampled in-vivo trials.

$$p(\boldsymbol{y_i}|\boldsymbol{x_i}) = (2\pi\sigma^2)^{-K_i/2}\ \exp\left(-\frac{1}{2\sigma^2}\left|\left|\boldsymbol{y_i} - \mathbf{F}_{\boldsymbol{u_i}}\boldsymbol{x_i}\right|\right|^2\right) \qquad \text{Eq. 4.17}$$

$$p(\boldsymbol{x_i}|c, d) = \prod_{j=1}^{N} \int_0^{\infty} N\left(x_j|0\alpha_j^{-1}\right) \Gamma\left(\alpha_j|c, d\right) d\alpha_i \qquad \text{Eq. 4.18}$$

Point estimates for the hyper-parameters $\boldsymbol{\alpha}$ are determined by maximizing the logarithm probability in Eq. 4.19. This process ensures that the hyper-parameters $\boldsymbol{\alpha}$ are estimated from both the simulated data and the in-vivo spectral data.

$$\boldsymbol{L}(\boldsymbol{\alpha_i}) = \sum_{\boldsymbol{i=1}}^{\mathbf{L}} \log \int p(\boldsymbol{y_i}|\mathbf{x_i}, \alpha_0)\, p(\mathbf{x_i}|\boldsymbol{\alpha_i}, \alpha_0)\, p(\alpha_0|\mathrm{a}, \mathrm{b}) dx_i\, d\alpha_0 \qquad \text{Eq. 4.19}$$

The implementation of this algorithm is done by a sequential greedy algorithm explained in [60] that starts with a single basis vector in the FT operator $\mathbf{F_u}$. A basis

vector is added if it gives the greatest increase in logarithm likelihood, and basis vectors already present are either updated or deleted if that gives the greatest increase in log-likelihood.

4.4 Evaluation of MT Bayesian CS

Using SPINEVOLUTION, seven brain metabolites [18], N-Acetyl-Aspartate (NAA), creatine (Cr), choline (Cho), glutamate (Glu), glutamine (Gln), myo-Inositol (mI), lactate (Lac) and water were simulated in a uniformly under-sampled, 17-t_1 step CTPRESS experiment with non-interfering aliasing as proposed by Mayer et al [42]. These fully sampled simulated spectra are added (ratio = 1:1:1:1:1:1:1:1) and later used for regularization in MT-Bayesian CS to aid in reconstruction of under-sampled data.

The simulated spectra were also combined in physiological ratios of 10.3mM NAA, 9.95mM total Cr, 1.63mM total Cho, 12mM Glu, 3mMGln, 6mMmyo-Inositol and 0.4mM Lac to constitute a simulation of the in-vivo trial. The 2D spectral data was under-sampled by 4 in the t_1 dimension as determined by a random draw from a uniform distribution, and Gaussian noise was added so that peak $SNR_{NAA} = 68$ in the 2D spectrum.

A 17-step CTPRESS CSI experiment with fast spiral encoding was applied in vivo on a 3.0 T MRI scanner (Siemens AG, Erlangen, Germany) using a 32 channel head coil. Shown in Figure 4-1, the PRESS box was applied for excitation of a rectangular volume of 8cm x 8cm in a FOV of 24cm x 24cm with slice thickness = 2cm. The 17-step 2D experiment was averaged twice for a total scan time of 4:40min. 2D spectral data was taken from a 4.5-cc voxel at the gray matter location in Figure 4-1 and retrospectively under-sampled in the t_1 dimension by R = 4.

Reconstructions of the under-sampled simulated and in-vivo 2D spectra were obtained via four methods**: i)** solution via an l_1 regularized formulation [62], **ii)** least squares

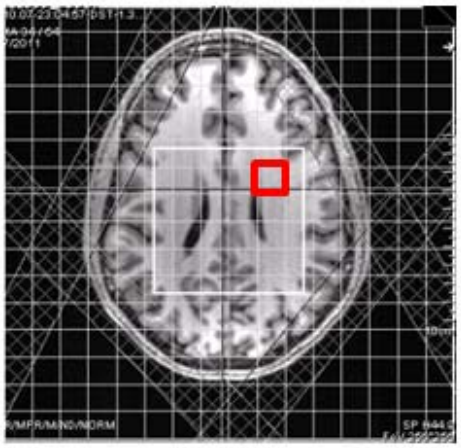

Figure 4-1: Anatomical MP-RAGE with prescribed Outer Volume Suppression (OVS) pulses for fat suppression. The white box indicates the excited volume. 2D spectral data from the voxel outlined in red is retrospectively under-sampled and reconstructed with MT Bayesian CS

fitting, **iii)** Single Task Bayesian CS and **iv)** MT Bayesian CS. The solution via an l_1 regularized formulation is reproduced in Eq. 4.20 where $\boldsymbol{y}$ contains under-sampled data, $\mathbf{F_u}$ is the under-sampled FT, and $\boldsymbol{x}$ is the reconstructed data. The under-sampled data, $\boldsymbol{y}$ was normalized across the 2D spectra and $\lambda = 0.005$ was chosen to balance between measurement consistency and enforced sparsity.

$$\boldsymbol{x'} = \text{argmin}_{\boldsymbol{x}} \|\mathbf{F_u}\boldsymbol{x} - \boldsymbol{y}\|_2 + \lambda\|\boldsymbol{x}\|_1 \qquad \text{Eq. 4.20}$$

Eq. 4.21 parameterizes $\boldsymbol{x}$ with the simulated metabolite spectra e.g.Cr_{sim} so that the reconstruction of $\boldsymbol{x}$ via least squares fitting in Eq. 4.22 is equivalent to solving for the weights $C_{metabolite}$ of the individual spectra.

$$\boldsymbol{x} = C_{NAA}NAA_{sim} + C_{Cr}Cr_{sim} + C_{Cho}Cho_{sim} + C_{Glu}Glu_{sim} + C_{Gln}Gln_{sim} + C_{mI}mI_{sim} + C_{Lac}Lac_{sim} \qquad \text{Eq. 4.21}$$

$$\boldsymbol{x}' = \text{argmin}_{\boldsymbol{x}} \|\mathbf{F}_{\boldsymbol{u}}\boldsymbol{x} - \boldsymbol{y}\|_2 \quad \text{Eq. 4.22}$$

The mean for the posterior distribution of $\boldsymbol{x}$, $\boldsymbol{\mu}$ is taken as its best estimate in both ST and MT Bayesian CS. In ST Bayesian CS, the estimation of $\boldsymbol{\alpha}$ is conditioned only on the under sampled spectra, while in MT Bayesian CS, the estimation of $\boldsymbol{\alpha}$ is conditioned on both the under-sampled spectra and the fully sampled simulated spectra.

4.4.1 Results

Reconstructed data was compared with the fully-sampled noise-frees data, and root mean square error of the diagonal decoupled spectra (RMSE) was computed as an error metric. The under-sampled CT-PRESS experiment and subsequent reconstruction was repeated over 20 noise realizations and 5 random under-sampling masks for 100 trials. Zero-filled spectral data is included as a comparison for the reconstruction methods.

4.4.1.1 Simulated Data

Figure 4-2 compares the diagonal decoupled spectrum from the noise-free fully-sampled 2D CT-PRESS spectrum and the diagonal spectra from CT-PRESS spectra reconstructed with different methods. Figure 4-3 shows the associated RMSE taken from 1.25ppm-4.25ppm of the reconstructed diagonal spectra. The insufficient recovery of spectral peaks explains the high RMSE from the reconstruction via zero filling of spectral data. In all four other reconstruction methods, major peaks of NAA, Cr, Cho, mI and Glu were recovered. However the low-SNR peaks of Glu, NAA+Gln and Glu+Gln between 2.25ppm-2.35ppm, 2.35ppm-2.47ppm and 3.69ppm-3.80ppm were best recovered by least squares fitting and MT Bayesian CS, where some form of prior spectral information was incorporated. Reconstruction via least squares fitting has the

lowest RMSE because the same simulated set of metabolite spectra that constituted the under-sampled data were also used in the parameterization of $\boldsymbol{x}$ in Eq. 4.21.

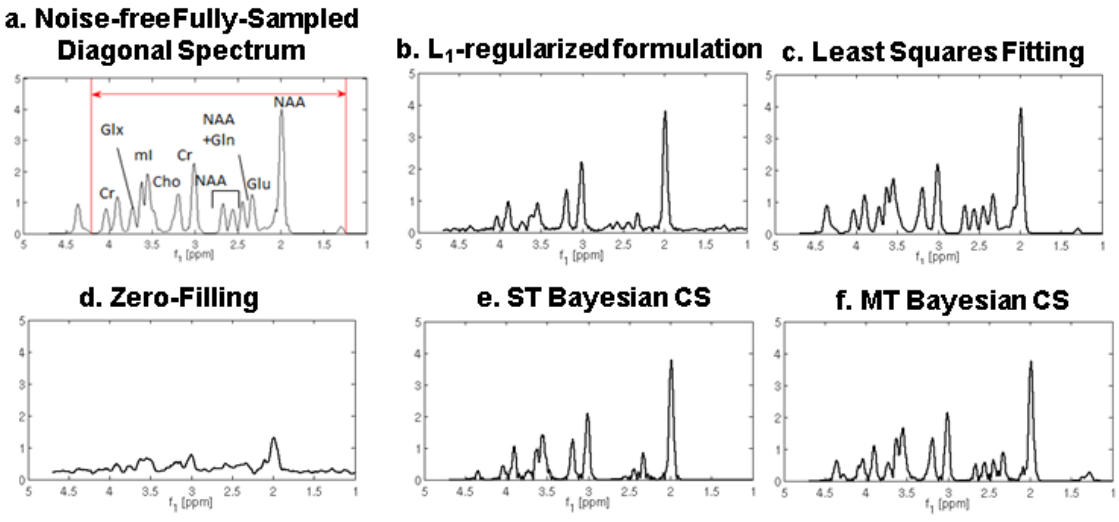

Figure 4-2: (a) Diagonal spectrum from noise-free fully sampled simulated 2D CT-PRESS spectrum (b)-(f) 1D diagonal spectra from reconstructed 2D CT-PRESS spectra. Glu, NAA and Gln peaks are only seen in (c) and (f)

Figure 4-3: Mean RMSE of diagonal spectra from reconstructed 2D CT-PRESS spectra. Reconstructions by least squares fitting have the lowest mean RMSE. MT Bayesian CS reconstructions have the next lowest mean RMSE.

4.4.1.2 In-Vivo Data

Figure 4-4a shows the diagonal decoupled spectrum from the fully-sampled 2D CT-PRESS spectrum ofs a 4.5cc gray matter voxel, and Figure 4-4b-f show the diagonal spectra from reconstructed 2D CT-PRESS spectra. The associated RMSE taken from 1.25ppm-4.25ppm of the diagonal spectra are displayed in Figure 4-5. Again, simple zero-filling cannot recover spectral peaks sufficiently. Major peaks of NAA, Cr, Cho were recovered by all four methods of solution, but the low-SNR peaks of Glu, NAA+Gln and Glu+Gln between 2.25ppm-2.35ppm, 2.35ppm-2.47ppm and 3.69ppm-successfully recovered by MT Bayesian CS. Least squares fitting failed to recover the metabolite peaks and their relative amplitudes while reconstruction with MT Bayesian CS recovered the metabolites peaks and gave the lowest RMSE.

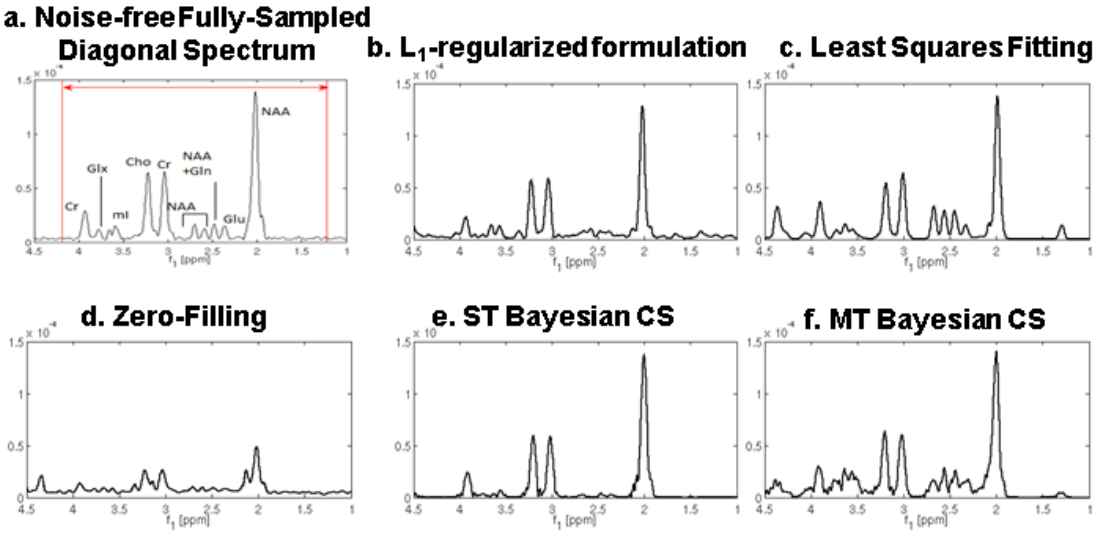

Figure 4-4: (a) Diagonal spectrum from noise-free fully sampled invio 2D CT-PRESS spectrum (b)-(f) 1D diagonal spectra from reconstructed 2D CT-PRESS spectra. Glu, NAA and Gln peaks are best reconstructed in (f)

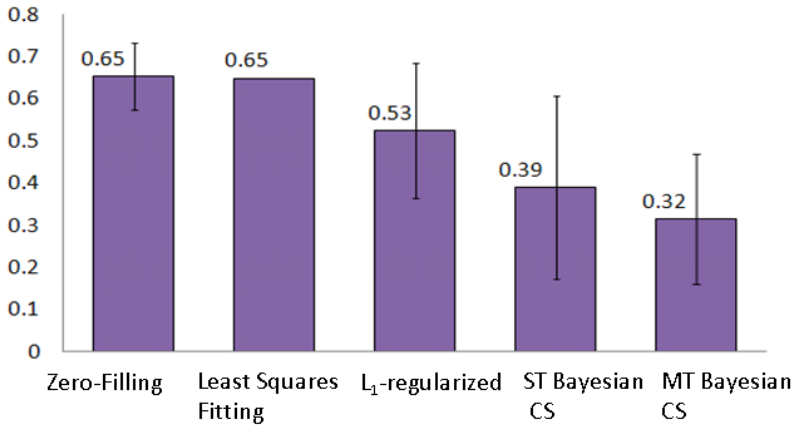

Figure 4-5: Mean RMSE of diagonal spectra from reconstructed 2D CT-PRESS spectra. Reconstructions by least squares fitting have the lowest mean RMSE. MT Bayesian CS reconstructions have the next lowest mean RMSE.

4.4.2 Discussion

Least squares fitting with the parameterization of $\boldsymbol{x}$ using simulated spectra did not sufficiently recover the low-SNR peaks of Glu, NAA+Glu and Glu+Gln because the simulated set of metabolite spectra does not accurately model the different relative amplitudes of spectral peaks from the same metabolites or their chemical shifts. Figure 4-6 shows the simulated diagonal spectra from individual metabolites overlaid onto the diagonal spectra from the in-vivo trial. The relative amplitudes of the peaks arising from simulated NAA do not match the peaks from NAA in the in-vivo trial, resulting in unsatisfactory fitting of the under-sampled in-vivo data. For improved reconstruction with least-squares fitting, factors such as relative amplitude differences from resonances of the same metabolite, B_0 and B_1 inhomogeneities, line-width and chemical shift variations, and background macromolecular signal can be included in the parameterization of x, like in the 1D metabolite spectra fitting and quantification software LCModel.

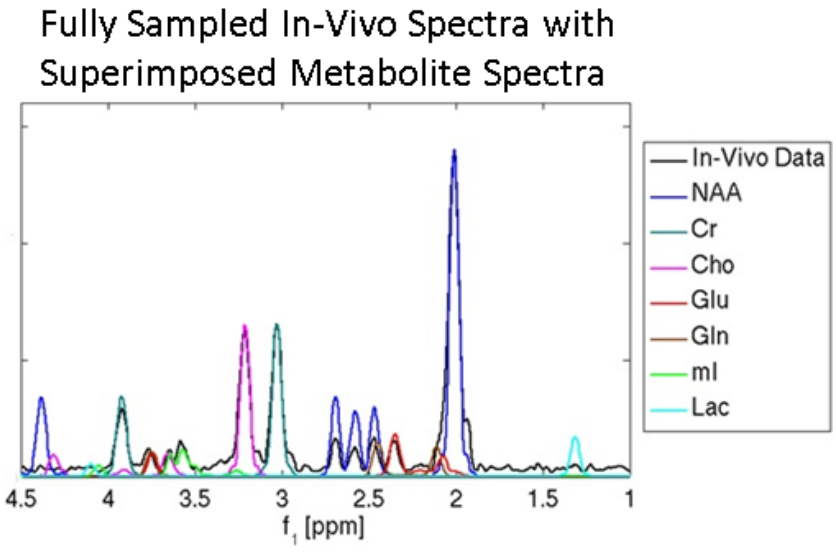

Figure 4-6: Individual Metabolite Spectra superimposed on in-vivo spectra show insufficient modeling of the parametric model. Relative amplitudes of frequency peaks from NAA are different from that of the in-vivo spectra.

MT Bayesian CS performed better because it is a hierarchical Bayesian model and does not impose strict correlation between the simulated spectral data and the in-vivo under-sampled data. Instead, the common priors α are learned from both the under-sampled in-vivo spectral data and the fully sampled simulated data, from which the best estimate for the in-vivo data is determined. So inaccurate modeling in the simulated spectra that result in shifted frequency peaks locations or different relative amplitudes from resonances of the same metabolite do not adversely affect the reconstruction.

4.5 Parameters for Noise Modeling in MT Bayesian CS

In MT Bayesian CS, a Gamma prior is defined over the noise precision term α_0 (Eq. 4.12), so that an inverse Gamma prior is introduced on σ^2

$$\mathrm{E}(\sigma^2) = \frac{b}{a-1} \qquad \text{Eq. 4.23}$$

$$\mathrm{Var}(\sigma^2) = \frac{b}{(a-1)^2(a-2)} \qquad \text{Eq. 4.44}$$

Previous reconstructions using MT Bayesian CS favor no a priori noise precision where $a = b = 0$, leading to the least informative prior. In this section, values for parameters a and b are explored for improved reconstruction of low SNR data.

Seven brain metabolites of NAA, Cr, Cho, Glu, Gln, mI, Lac and water were again simulated with SPINEVOLUTION in a 17 step CT-PRESS experiment. The fully sampled simulated spectra of the brain metabolites were weighted equally and summed, and used for regularization in MT-Bayesian CS. The simulated spectra were also combined in the ratio of 10.3 mM NAA, 9.95 mM total Cr, 1.63 mM total Cho, 12 mM Glu, 3mM Gln, 6mM myo-Inositol, 0.4mM Lac to constitute a simulation of an in-vivo trial. This spectrum is under-sampled in the t_1 dimension by a factor of R = 2 and R=4 as determined by a random draw from a uniform distribution. Gaussian noise of $\sigma^2 = 0.0025$ was added such that peak $\mathrm{SNR}_{\mathrm{NAA}} = 20$ in the 2D spectrum. Figure 4-7a and b show the diagonal spectra from the fully-sampled 2D CT-PRESS experiment before and after the addition of noise. Diagonal spectra are formed from summing the magnitude 2D CT-PRESS spectra along the diagonal, so that Figure 4-7b has a magnitude offset due to noise.

Spectra were reconstructed for $a = 1778$, and $b = 0.044$ to 40, so that $\mathrm{E}[\sigma^2]$ ranges from 2.5E-5 to 0.0225 and $\mathrm{Var}[\sigma^2]$ is small and range from 7.9E-12 to 7.1E-9. Focusing on the low-SNR peaks of Glu, NAA+Gln, and Glx between 2.25ppm-2.35ppm, 2.35ppm-2.47ppm and 3.69ppm-3.80ppm respectively, reconstructed spectra were compared to the fully-sampled baseline spectra and RMSE evaluated for 20 noise

realizations and 5 under-sampling realizations. We attempt to determine empirically the value of b that gives the minimum RMSE for future inclusion of *a priori* noise precision in the MT Bayesian CS reconstruction.

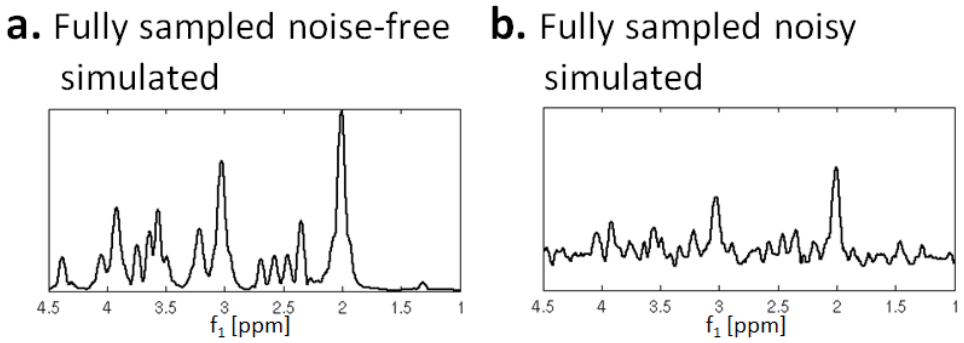

Figure 4-7: Diagonal spectra from (a) noise-free and (b) noisy simulated 2D CT-PRESS spectra. Gaussian noise was added to the 2D spectrum so that peak $SNR_{NAA} = 20$

Assuming ideally phased priors, *Real(x)* and *Imag(x)* were solved for with MT Bayesian CS using the real and imaginary parts of the simulated spectra. To approximate scanning conditions where phase priors are uncertain, *Abs(m_i)* and *Phase(m_i)* are solved for with MT Bayesian CS using the magnitude of the simulated spectra and ST Bayesian CS respectively.

4.5.1 Results and Discussion

Figure 4-8 shows mean RMSE of the reconstructed spectra taken over 100 random trials assuming ideally phased priors. The minimum RMSE is at $b_{opt} = 4.443$ for both R=2 and R=4 under-sampling factors. $b_{opt} = 4.443$ corresponds to $E[\sigma^2] = 0.0025$, which matched the noise of $\sigma^2 = 0.0025$ added to the simulated spectra. Small values of b resulted in small values for $E[\sigma^2]$, limiting the de-noising feature of MT Bayesian CS reconstructions. On the other hand, large values of b assume more noise than present in the under-sampled spectra which lead to dropouts of Glu and Gln peaks in the CS reconstructions. Figure 4-9a shows the diagonal spectra formed from

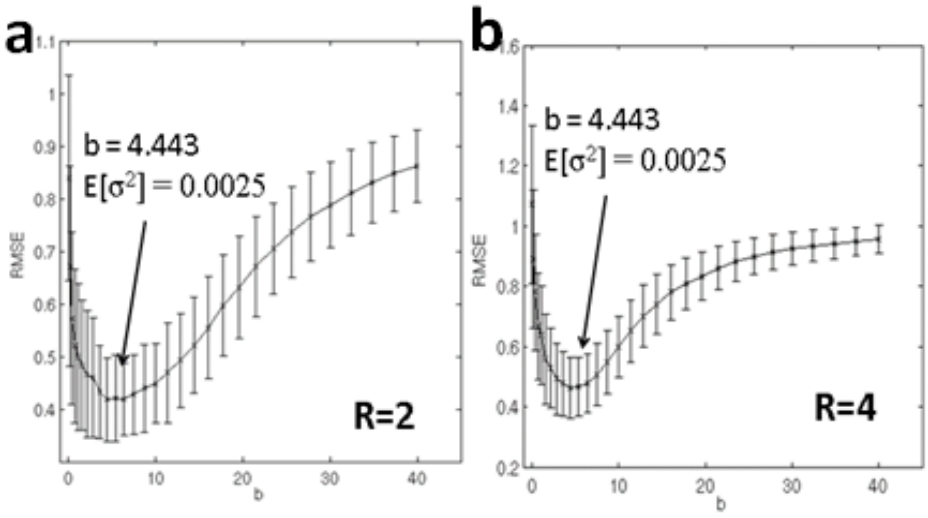

Figure 4-8: RMSE evaluated for low-SNR peaks evaluated with different values of b for under-sampling factor of R = 2 and R = 4 using MT Bayesian CS with perfectly phase priors.

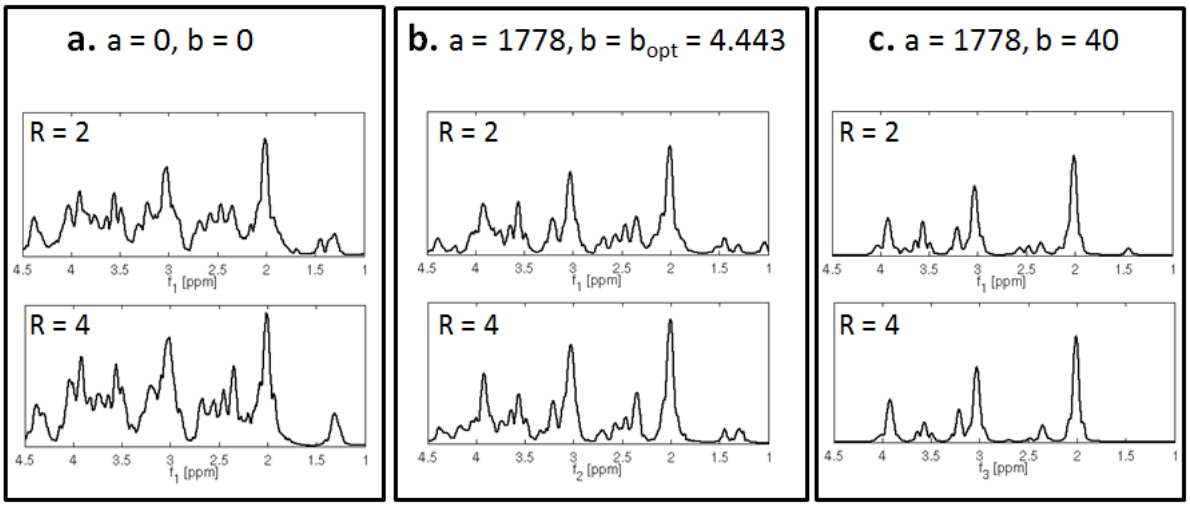

Figure 4-9: Diagonal spectra from reconstructed 2D CT-PRESS spectra with different values of a and b for under-sampling factors R = 2 and R = 4.

the reconstructed 2D spectra for $a = 0$ and $b = 0$ without *a priori* noise precision, and Figure 4-9b demonstrates the successful reconstruction of Glu and Gln peaks in the

diagonal spectra formed with the suggested choice of $a = 1778$ and b = 4.443 that best models $\sigma^2 = 0.0025$ added to the simulated spectra.

Figure 4-10a and b show mean RMSE taken over 100 random trials assuming non-ideal scanning conditions where phase priors are uncertain. The minimum RMSE corresponds to $E[\sigma^2] = 0.0049$ for R = 2 and $E[\sigma^2] = 0.010$ for R = 4 which do not correspond to the noise of $\sigma^2 = 0.0025$ added to the simulated spectra. We postulate that this discrepancy is due to insufficient modeling of Rayleigh noise with non-zero mean in the reconstruction of *Abs(m_i)* with MT Bayesian CS.

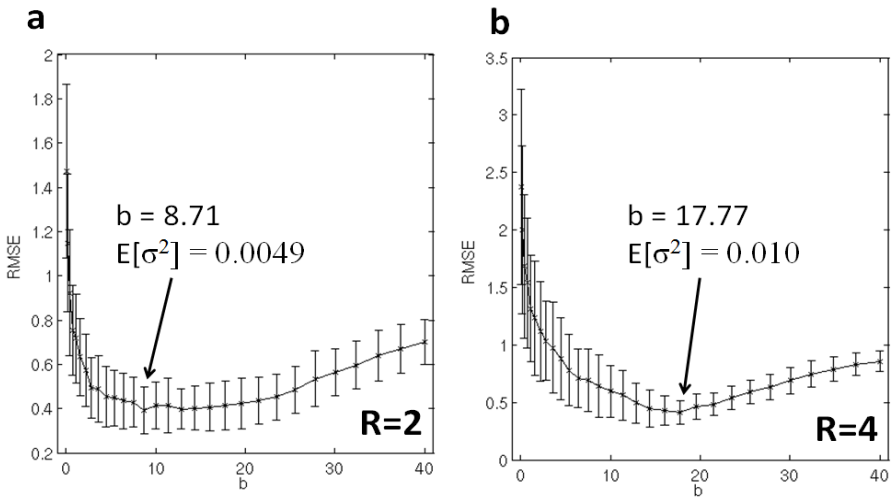

Figure 4-10: RMSE evaluated for low-SNR peaks evaluated with different values of b for under-sampling factor of R = 2 and R = 4 using MT Bayesian CS with imperfect phase information.

4.6 Conclusion

The performance of MT Bayesian CS is compared with other methods for reconstruction of under-sampled CT PRESS. In the absence of information about phase, chemical shift or line width variations, MT Bayesian CS was most successful at reconstructing low-SNR peaks of Glu, NAA+Gln, and Glu+Gln. An extension of this work is to compare MT Bayesian CS with other methods based on algorithms such as Simultaneous Orthogonal Matching Pursuit [71] and M-FOCal Underdetermined

System Solver (FOCUSS) [72], which similarly exploit similarities in multiple measurements to improve reconstruction.

Phase variations common in spectroscopy data complicate the assignment of values for hyper-parameters a and b based on estimated noise variance. Future work includes further exploration of noise modeling parameters for reconstruction of magnitude spectra with MT Bayesian CS where phase priors are uncertain.

Chapter 5

Conclusions and Future Work

5.1 Conclusions

1D MRS spectra suffer from substantial spectral overlap between individual metabolite signals that hamper the detection and quantification of metabolites. 2D MRS methods such as the 17-step CT-PRESS spread J-coupling information in a 2D frequency space for increased spectral dispersion and the opportunity for effective homonuclear decoupling. However, the additional dimension increases total minimum scan time which prohibits 2D MRS implementations for high-resolution spectroscopic imaging purposes.

This dissertation presents the 17-step CT-PRESS method implemented with spiral encoding for a high resolution 1.11cc voxel size in-vivo human scan. The additional SNR presented by the 32-channel receive coil array in the cortical tissue near the skull is traded off for the small voxel size and the short total scan time of 3:32min with just one average. The lipid minimization algorithm presented in this thesis

successfully removes lipid contamination, so that decoupled peaks of Glu, NAA and Gln are detectable in these cortical regions with good sensitivity.

Another contribution of this thesis is the exploration of reducing scan times in 2D MRS experiment via random under-sampling in the indirect time dimension and subsequent reconstruction with Multi-Task Bayesian Compressed Sensing (MT Bayesian CS). The reconstruction of under-sampled data was improved with the incorporation of simulated prior spectral information for regularization. In the case of inadequate simulated spectra, spectral quality obtained with reconstruction by MT Bayesian CS remained good because MT Bayesian CS did not impose strict correlation between simulated spectra and in-vivo under-sampled data. As spectroscopy data have intrinsically low SNR, hyper-parameters a and b n MT Bayesian CS were modified to match the expected noise characteristics in simulated trials. In the ideal case of perfectly phased prior spectral information, the hyper-parameters which matched the noise statistics gave the best reconstructions.

5.2 Future Work

5.2.1 2D MR Spectroscopic Imaging with Lipid Minimization

The availability of multi-channel coils such as the 64-channel coil on the Siemens Skyra system (Siemens, Erlangen, Germany) and the corresponding increase in SNR allows for even greater trade-offs for scan-time and voxel size. SNR increases with B_0 field strength and the CT-PRESS experiment can potentially be done at field strengths of 7T and higher. Imaging at 7T however introduces challenges such as more severe B_1 and B_0 inhomogeneities and restricted RF excitation due to specific absorption rate (SAR) constraints.

Other 2D MRS methods such as COSY and 2D JPRESS could also be implemented with spiral encoding and applied with the lipid minimization algorithm. The implementation of 2D JPRESS with spiral encoding for cortical metabolites detection opens up clinical applications due to the availability of fitting and quantification software ProFit [73] designed for spectral quantification of 2D JPRESS spectra.

5.2.2 Compressed Sensing for 2D MRS

MT Bayesian CS incorporates prior spectral information to regularize and improve the reconstruction of under-sampled 2D MRS data. It would be noteworthy to compare the performance of MT Bayesian CS with other algorithms that exploit similarities in multiple measurements, whether simulated or experimental, for improved reconstruction. When modifying hyper-parameters for noise modeling, in the presence of phase variations and imperfect phase information, the hyper-parameters that gave the best reconstructions did not match the noise statistics added to the under-sampled simulated spectra. In this case, future work has to be done to explore the relationship between the hyper-parametes and the Rayleigh noise statistics of the magnitude spectrum reconstructed with MT Bayesian CS.

Chapter 6

Bibliography

1. Rajanayagam, V., et al., *Proton MR spectroscopy of childhood adrenoleukodystrophy.* AJNR Am J Neuroradiol, 1996. **17**(6): p. 1013-24.

2. Tzika A.A., et al., *Childhood adrenoleukodystrophy: assessment with proton MR spectroscopy.* Radiology, 1993. **189**(2): p. 467-480.

3. Ratai, E., et al., *Seven-Tesla proton magnetic resonance spectroscopic imaging in adult X-linked adrenoleukodystrophy.* Arch Neurol, 2008. **65**(11): p. 1488-94.

4. Pfefferbaum, A., et al., *In vivo brain concentrations of N-acetyl compounds, creatine, and choline in Alzheimer disease.* Arch Gen Psychiatry, 1999. **56**(2): p. 185-92.

5. Mohanakrishnan, P., et al., *An in vitro 1H nuclear magnetic resonance study of the temporoparietal cortex of Alzheimer brains.* Exp Brain Res, 1995. **102**(3): p. 503-10.

6. Schuff, N., et al., *Changes of hippocampal N-acetyl aspartate and volume in Alzheimer's disease. A proton MR spectroscopic imaging and MRI study.* Neurology, 1997. **49**(6): p. 1513-21.

7. Klunk, W.E., et al., *N-acetyl-L-aspartate and other amino acid metabolites in Alzheimer's disease brain: a preliminary proton nuclear magnetic resonance study.* Neurology, 1992. **42**(8): p. 1578-85.

8. Bloch, F., *Nuclear Induction.* Physics Review, 1946. **70**: p. 460-473.

9. Purcell, E., *Resonance absorption by nuclear magnetic moments in a solid.* 69, 1946: p. 37-38.

10. Mugler, J.P., III and J.R. Brookeman, *Three-dimensional magnetization-prepared rapid gradient-echo imaging (3D MP RAGE).* Magn Reson Med, 1990. **15**(1): p. 152-7.

11. Woolrich, M.W., et al., *Bayesian analysis of neuroimaging data in FSL.* Neuroimage, 2009. **45**(1 Suppl): p. S173-86.

12. Smith, S.M., et al., *Advances in functional and structural MR image analysis and implementation as FSL.* Neuroimage, 2004. **23 Suppl 1**: p. S208-19.

13. Smith, S.M., *Fast robust automated brain extraction.* Hum Brain Mapp, 2002. **17**(3): p. 143-55.

14. De Stefano, N., P.M. Matthews, and D.L. Arnold, *Reversible decreases in N-acetylaspartate after acute brain injury.* Magn Reson Med, 1995. **34**(5): p. 721-7.

15. Chard, D.T., et al., *Brain metabolite changes in cortical grey and normal-appearing white matter in clinically early relapsing-remitting multiple sclerosis.* Brain, 2002. **125**(Pt 10): p. 2342-52.

16. Tsai, G. and J.T. Coyle, *N-acetylaspartate in neuropsychiatric disorders.* Prog Neurobiol, 1995. **46**(5): p. 531-40.

17. Rudkin, T.M. and D.L. Arnold, *Proton magnetic resonance spectroscopy for the diagnosis and management of cerebral disorders.* Arch Neurol, 1999. **56**(8): p. 919-26.

18. Govindaraju, V., K. Young, and A.A. Maudsley, *Proton NMR chemical shifts and coupling constants for brain metabolites.* NMR Biomed, 2000. **13**(3): p. 129-53.

19. Michael, N., et al., *Acute mania is accompanied by elevated glutamate/glutamine levels within the left dorsolateral prefrontal cortex.* Psychopharmacology (Berl), 2003. **168**(3): p. 344-6.

20. Frye, M.A., et al., *Increased anterior cingulate/medial prefrontal cortical glutamate and creatine in bipolar depression.* Neuropsychopharmacology, 2007. **32**(12): p. 2490-9.

21. J H Duyn, et al., *Multisection proton MR spectroscopic imaging of the brain.* Radiology, 1993. **188**: p. 277-282.

22. Le Roux, P., et al., *Optimized outer volume suppression for single-shot fast spin-echo cardiac imaging.* J Magn Reson Imaging, 1998. **8**(5): p. 1022-32.

23. Luo, Y., et al., *BISTRO: an outer-volume suppression method that tolerates RF field inhomogeneity.* Magn Reson Med, 2001. **45**(6): p. 1095-102.

24. Tran, T.K., et al., *Very selective suppression pulses for clinical MRSI studies of brain and prostate cancer.* Magn Reson Med, 2000. **43**(1): p. 23-33.

25. Bydder, G.M. and I.R. Young, *MR imaging: clinical use of the inversion recovery sequence.* J Comput Assist Tomogr, 1985. **9**(4): p. 659-75.

26. Ebel, A., V. Govindaraju, and A.A. Maudsley, *Comparison of inversion recovery preparation schemes for lipid suppression in 1H MRSI of human brain.* Magn Reson Med, 2003. **49**(5): p. 903-8.

27. Spielman, D.M., et al., *Lipid-suppressed single- and multisection proton spectroscopic imaging of the human brain.* J Magn Reson Imaging, 1992. **2**(3): p. 253-62.

28. Balchandani, P. and D. Spielman, *Fat suppression for 1H MRSI at 7T using spectrally selective adiabatic inversion recovery.* Magn Reson Med, 2008. **59**(5): p. 980-8.

29. J Lee and E. Adalsteinsson, *Subcutaneous lipid suppression via variable-density spiral sampling for full cortical coverage in chemical shift imaging*, in *Proceedings of the 17th Meeting of ISMRM*2009: Honolulu, Hawaii, USA.

30. Hore, P., J. Jones, and S. Wimperis, *NMR: The Toolkit.* Oxford Chemistry Primers2000, Great Britain: Oxford Science Publications.

31. Hore, P., *Nuclear Magnetic Resonance.* Oxford Chemistry Primers1995, Great Britain: Oxford Science Publications.

32. Rothman, D.L., et al., *Localized 1H NMR spectra of glutamate in the human brain.* Magn Reson Med, 1992. **25**(1): p. 94-106.

33. McKinnon, G.C. and P. Bosiger, *Localized double-quantum filter and correlation spectroscopy experiments.* Magn Reson Med, 1988. **6**(3): p. 334-43.

34. Haase A, S.N., Norris D, Leibfritz D. *Localized COSY NMR spectroscopy.* in *7th Meeting of ISMRM.* 1987.

35. Thomas, M.A., et al., *Localized two-dimensional shift correlated MR spectroscopy of human brain.* Magn Reson Med, 2001. **46**(1): p. 58-67.

36. Dreher, W. and D. Leibfritz, *On the use of two-dimensional-J NMR measurements for in vivo proton MRS: measurement of homonuclear decoupled spectra without the need for short echo times.* Magn Reson Med, 1995. **34**(3): p. 331-7.

37. Ryner, L.N., J.A. Sorenson, and M.A. Thomas, *Localized 2D J-resolved 1H MR spectroscopy: strong coupling effects in vitro and in vivo.* Magn Reson Imaging, 1995. **13**(6): p. 853-69.

38. Aue WP, K.J., Ernst RR, *Homonuclear broad band decoupling and two-dimensional J-resolved NMR spectroscopy.* Magnetic Resonance in Medicine, 1976. **1999**(41): p. 8-12.

39. Hurd, R., et al., *Measurement of brain glutamate using TE-averaged PRESS at 3T.* Magn Reson Med, 2004. **51**(3): p. 435-40.

40. Dreher, W. and D. Leibfritz, *Detection of homonuclear decoupled in vivo proton NMR spectra using constant time chemical shift encoding: CT-PRESS.* Magn Reson Imaging, 1999. **17**(1): p. 141-50.

41. Mayer, D. and D.M. Spielman, *Detection of glutamate in the human brain at 3 T using optimized constant time point resolved spectroscopy.* Magn Reson Med, 2005. **54**(2): p. 439-42.

42. Mayer, D., et al., *Fast CT-PRESS-based spiral chemical shift imaging at 3 Tesla.* Magn Reson Med, 2006. **55**(5): p. 974-8.

43. Brown, T.R., B.M. Kincaid, and K. Ugurbil, *NMR chemical shift imaging in three dimensions.* Proc Natl Acad Sci U S A, 1982. **79**(11): p. 3523-3526.

44. Howe, F.A., et al., *Proton spectroscopy in vivo.* Magn Reson Q, 1993. **9**(1): p. 31-59.

45. A. A. Maudsley, S.K.H., *Spatially resolved high resolution spectroscopy by four-dimensional NMR.* Magn Reson Med, 1983. **51**: p. 147-152.

46. Mansfield, P., *Spatial mapping of the chemical shift in NMR.* Magn Reson Med, 1984. **1**(3): p. 370-86.

47. Posse, S., et al., *High speed 1H spectroscopic imaging in human brain by echo planar spatial-spectral encoding.* Magn Reson Med, 1995. **33**(1): p. 34-40.

48. Posse, S., et al., *Proton echo-planar spectroscopic imaging of J-coupled resonances in human brain at 3 and 4 Tesla.* Magn Reson Med, 2007. **58**(2): p. 236-44.

49. Adalsteinsson, E., et al., *Volumetric spectroscopic imaging with spiral-based k-space trajectories.* Magn Reson Med, 1998. **39**(6): p. 889-98.

50. B. Gagoski, M.H., J. Polimeni, G. Krueger, E-M. Ratai, G. Wiggins, U. Boettcher, J. Lee, F. Eichler, S. Roell and E. Adalsteinsson. *Volumetric chemical shift imaging with 32-channel receive coil at 3T with online gridding reconstruction.* in *Proceedings of the 16th Meeting of ISMRM.* 2008.

51. Lipnick, S., et al., *Echo planar correlated spectroscopic imaging: implementation and pilot evaluation in human calf in vivo.* Magn Reson Med, 2010. **64**(4): p. 947-56.

52. R. Nagarajan, J.F., D. Margolis, S. Raman, M. K. Sarma, and M. A. Thomas, *Echo planar based J resolved and correlated spectroscopic imaging of human prostate using external coil.* Proceedings of the 18th Meeting of ISMRM, 2011: p. 2801.

53. Verma, G., et al., *Implementation of multi-echo-based correlated spectroscopic imaging and pilot findings in human brain and calf muscle.* J Magn Reson Imaging, 2011. **34**(2): p. 262-9.

54. Mayer, D., W. Dreher, and D. Leibfritz, *Fast echo planar based correlation-peak imaging: demonstration on the rat brain in vivo.* Magn Reson Med, 2000. **44**(1): p. 23-8.

55. Dong-Hyun Kim, 2 Roland Henry,1 and Daniel M. Spielman3, *Fast Multi-voxel Two-dimensional Spectroscopic Imaging at 3T.* Magn Reson Imaging, 2007. **25**(8): p. 1155-1161.

56. Wiggins, G.C., et al., *32-channel 3 Tesla receive-only phased-array head coil with soccer-ball element geometry.* Magn Reson Med, 2006. **56**(1): p. 216-23.

57. J lee , E.A. *Iterative CSI reconstruction with high-resolution spatial priors for improved lipid suppression.* in *Proceedings of the 18th Meeting of ISMRM.* 2010.

58. Wiggins, G.C., et al., *96-Channel receive-only head coil for 3 Tesla: design optimization and evaluation.* Magn Reson Med, 2009. **62**(3): p. 754-62.

59. Veshtort, M. and R.G. Griffin, *SPINEVOLUTION: a powerful tool for the simulation of solid and liquid state NMR experiments.* J Magn Reson, 2006. **178**(2): p. 248-82.

60. Shihao Ji, D.D., and Lawrence Carin, *Multi-Task Compressive Sensing.* IEEE Trans. Signal Processing, 2009. **57**(1): p. 92-106.

61. Shihao Ji, Y.X., and Lawrence Carin, *Bayesian Compressive Sensing.* IEEE Trans. Signal Processing, 2008. **56**(6): p. 2346-2356.

62. Lustig, M., D. Donoho, and J.M. Pauly, *Sparse MRI: The application of compressed sensing for rapid MR imaging.* Magn Reson Med, 2007. **58**(6): p. 1182-95.

63. Provencher, S.W., *Estimation of metabolite concentrations from localized in vivo proton NMR spectra.* Magn Reson Med, 1993. **30**(6): p. 672-9.

64. Emmanuel Candes, J.R., and Terence Tao., *Robust uncertainty principles: Exact signal reconstruction from highly incomplete frequency information.* IEEE Transactions on Information Theory,, 2006. **52**: p. 489-509.

65. Donoho, D., *Compressed Sensing.* IEEE Transactions on Information Theory, 2006. **52**: p. 1289-1306.

66. Furuyama, J.K., et al., *Application of compressed sensing to multidimensional spectroscopic imaging in human prostate.* Magn Reson Med, 2012. **67**(6): p. 1499-505.

67. Mobli, M. and J.C. Hoch, *Maximum Entropy Spectral Reconstruction of Non-Uniformly Sampled Data.* Concepts Magn Reson Part A Bridg Educ Res, 2008. **32A**(6): p. 436-448.

68. Rovnyak, D., et al., *Accelerated acquisition of high resolution triple-resonance spectra using non-uniform sampling and maximum entropy reconstruction.* J Magn Reson, 2004. **170**(1): p. 15-21.

69. Hoch, J.C. and A.S. Stern, *Maximum entropy reconstruction, spectrum analysis and deconvolution in multidimensional nuclear magnetic resonance.* Methods Enzymol, 2001. **338**: p. 159-78.

70. Smith SA, L.T., Meier BH, Ernst RR., *Computer simulations in magnetic resonance. an object-oriented programming approach.* J Magn Reson Ser A, 1994. **106**: p. 75-105.

71. Tropp JA, G.A., Strauss MJ., *Algorithms for simultaneous sparse approximation. Part I: greedy pursuit.* Signal Processing, 2006. **86**(572-588).

72. Cotter SF, R.B., Engan K, Kreutz-Delgado K., *Sparse solutions to linear inverse problems with multiple measurement vectors.* IEEE Trans Signal Process, 2005. **53**: p. 2477-2488.

73. Schulte, R.F., Boesiger, P., *ProFit: two-dimensional prior-knowledge fitting of J-resolved spectra.* NMR Biomed, 2006. **19**(2): p. 255-63.

THIS PAGE INTENTIONALLY LEFT BLANK